Estimating the mass of tephra accumulated on roads to best manage the impact of volcanic eruptions: the example of Mt. Etna, Italy

Luigi Mereu[1,2], Manuel Stocchi[1*], Alexander Garcia[1], Michele Prestifilippo[3], Laura Sandri[1], Costanza Bonadonna[4] and Simona Scollo[3]

[1]Istituto Nazionale di Geofisica e Vulcanologia, Sezione di Bologna, 40100 Bologna, Italy
[2]CETEMPS Center of Excellence, University of L'Aquila, 67100 L'Aquila, Italy
[3]Istituto Nazionale di Geofisica e Vulcanologia, Osservatorio Etneo, Sezione di Catania, 95015 Catania, Italy
[4]Department of Earth Sciences, University of Geneva, 1205 Geneva, Switzerland
* Now at Department of Earth and Geoenvironmental Sciences, University of Bari "Aldo Moro", 70125 Bari, Italy

Correspondence to: Luigi Mereu (luigi.mereu@ingv.it)

To be submitted to NHESS

Abstract. Explosive eruptions release significant quantities of tephra, which can spread and settle on the ground, potentially leading to various types of damage and disruption to public infrastructure, including road networks. The quantification of the tephra load is, therefore, of significant interest to evaluate and reduce environmental and socio-economic impact, and for managing crises. Tephra dispersal and deposition is a function of multiple factors, including the mass eruption rate (MER), tephra characteristics (size, shape, density), top plume height (H_{TP}), grain size distribution (GSD) and local wind field. In this work we quantified the tephra mass deposited on the main road network on the east-southeast flanks of Mt. Etna (Italy), during lava fountains occurred in 2021, which are lava jets ejected into the air due to the rapid formation and expansion of gas bubbles within the molten rock, also reaching heights of hundreds of metres. We focused on road connections of municipalities significantly affected by these events such as Milo, Santa Venerina and Zafferana Etnea. First, we analysed a sequence of 39 short-lasting and intense Etna's lava fountains detected by the X-band weather radar, applying a volcanic ash radar retrieval approach that permits us to compute the main eruption source parameters (ESPs), such MER, H_{TP} and GSD. When radar measurements were unavailable for a specific event, we analysed images acquired both by the SEVIRI radiometer and by the visible and/or thermal infrared camera of the Istituto Nazionale di Geofisica e Vulcanologia, Osservatorio Etneo (Catania) to derive the main ESPs. Second, we used the computed ESPs as inputs to run two different

numerical models, Tephra2 and Fall3D, and reproduce tephra dispersal and accumulation on the road network. Finally, we produce, for the first time, georeferenced estimates of tephra mass deposited on the whole road network of three municipalities, allowing us to identify the main roads which have been mostly impacted by tephra accumulation, as well as to estimate the total mass of primary tephra that has been removed from roads. Such information represents a valuable input for planning and quick management of the short-term tephra load hazard for future Etna explosive events.

1 Introduction

The estimation of tephra mass deposited on the ground, following a volcanic explosive eruption, remains a key information that is not well-covered in the current literature. In fact, tephra dispersal and fallout is by far the most widespread volcanic hazard affecting both local and distal areas (Jenkins et al. 2015; Barsotti et al., 2018; Bonadonna et al. 2021b) including impact on public health (Baxter, 1990; Horwell and Baxter, 2006), roofs/building collapse (Spence et al., 2005), dangerous road conditions (Blong, 1996; Wilson et al., 2012; Jenkins et al., 2014; Blake et al., 2017), contamination of water reservoirs and vegetation (Wilson et al., 2012; Ágústsdóttir, 2015), damages to electrical infrastructure (Bebbington et al., 2008; Wardman et al., 2012; Wilson et al., 2012, Dominguez et al., 2021), transportation system disruptions (Casadevall, 1994; Guffanti et al., 2009; Wilson et al., 2012), and impact on telecommunication networks (Wilson et al., 2012). Even tephra associated with relatively small intensity eruptions may induce various disrupting effects on transport infrastructure such as aeroplane engine failure and visibility reduction during both primary tephra fall and ash remobilisation (Sarna-Wojcicki et al., 1981; Bonadonna et al., 2021b; Johnston and Daly, 1995; Wilson et al., 2014). In particular, tephra accumulation, although not causing significant physical damage on the road network, can cause wide disruption including reduction of skid resistance, obscuration of road markings and damage to car air filters (Blake et al., 2016, 2017). Tephra particles are also very abrasive with the degree of abrasiveness dependent on the hardness of the material forming the particles and their shape and angularity (Blong, 1984; Johnston, 1997; Labadie, 1994; Heiken et al., 1995; Miller and Casavedall, 1999; Gordon et al., 2005; Wilson et al., 2012; Blake et al., 2017). Road networks are critical for society under normal operating conditions and especially during emergencies (e.g. Bonadonna et al. 2021a; Hayes et al. 2022).

During volcanic eruptions, routes may be required for the evacuation of residents and to allow emergency services and civil protection personnel to access the affected areas. The road network is also crucial for both immediate and long-term recovery, including clean-up and disposal of pyroclastic material, and restoration of services and commerce (Blake et al., 2017).

In this work, for the first time, we quantify the tephra mass accumulated on the road network of east and south-east sectors of Etna, which were more affected during the sequence of explosive events of 2021. Usually, the eruptive sequences at Etna are characterised by short-lasting explosive events, with duration of few hours, separated by periods that can last from few hours to few days (Calvari et al., 2018; Andronico et al., 2021; Calvari et al., 2022a). Most studies on exposed critical

infrastructure have focussed on larger events and tephra-fallout accumulations greater than 10 kg/m^2 (Wilson et al., 2012, Blake et al., 2017; Scollo et al., 2013). However, areas around Etna are more frequently impacted by smaller tephra accumulation (Scollo et al., 2013). Limited quantitative data available for explosive activity have hampered a reliable quantification of the impact of the tephra deposition at Etna. To investigate its impact on road networks and better characterise its behaviour, we analysed a sequence of several lava fountains occurred between February 2021 and October 2021, focusing our analysis on 39 events that generated volcanic plumes dispersed by wind mostly towards the east-southeast flanks of the volcano (direction between 90 degrees and 130 degrees from North). These episodes began at the South East Crater (SEC) as initial Strombolian activity that, with time, evolved to lava fountain activity, also named paroxysm.

Remote sensing is routinely used for monitoring the eruptive activity of Etna; the Istituto Nazionale di Geofisica e Vulcanologia, Osservatorio Etneo (INGV-OE) runs a network of different remote sensing sensors both ground-based (such as thermal infrared and visible cameras) and satellite-based sensors (Scollo et al., 2019). An X-band weather radar located in Fontanarossa airport (Catania), which is part of the monitoring network of the Italian Department of Civil Protection (DPC) allows to monitor and analyse the Etna's eruptions as well (Marzano et al. 2020; Mereu et al. 2020). Using these sensors, we can observe in almost all the cases the temporal evolution of explosive activity and characterise it quantitatively in terms of mass eruption rate (MER) and top plume height (H_{TP}). These two parameters are among the main input variables for advection-dispersion models (Scollo et al., 2008a; Biass et al., 2017; Tadini et al., 2022; Takishita et al., 2021), such as Tephra2 and Fall3D (Bonadonna et al., 2005; Costa et al., 2006; Folch et al., 2009, 2020), which have been used in this work to simulate the tephra dispersion and calculate the deposit load at the ground. For each of the 39 events, we estimate the tephra deposited on the road network in order to identify the roads mostly exposed to tephra accumulation and to evaluate the ground mass load that is expected to be removed. Moreover, analysing the simulations done using both models, we investigate their sensitivity to variations of tephra granulometric characteristics and assess the associated uncertainties. The numerical output from a single simulation is a georeferenced map of tephra load, useful to analyse the impact of deposited tephra fallout on roads (Scollo et al., 2009; Scollo et al., 2013; Costa et al., 2012; Bonadonna et al., 2005; Barsotti et al., 2018; Bonadonna et al. 2021a).

Analysing tephra accumulation on roads is essential for planning effective responses during volcanic eruptions. By measuring the amount of tephra deposited during both single and multiple eruptions, we can identify which are the roads that are most affected. Moreover, the deposited tephra creates disruptions especially on main roads, considering the large stretches of roadway that may face hazardous driving conditions. This information helps estimate how much material needs to be disposed of and the costs involved in clean up operations. Studying the lava fountain events of Etna in 2021 provides valuable insights for future planning during similar events. By examining the past eruptions, we can predict tephra deposits, providing useful information to decision makers to develop better cleaning up strategies. Indeed, for future eruptions, it is important to consider creating a model that uses real-time data to improve predictions and clean up plans. Overall, this

research can help crisis management and enhance safety in volcanic regions. Additionally, recent regional legislation (DA n. 8/Gab. 22/04/2024, https://www.regione.sicilia.it) permits the use of the volcanic tephra for building applications; in this new framework, this study represents an initial effort to estimate the volume of tephra that may be reused rather than disposed of, transforming a potential problem into a resource.

The work is organised as follow: Section 2 provides a brief description of Etna's lava fountain activity; Section 3 presents ground- and satellite-based sensor data, along with the main eruption source parameters (ESPs) retrieved from them, and the methodology employed to analyse the model results; Section 4 validates the results against previously published data for a specific event (February 28th, 2021); Section 5 discusses the modelling outputs and provides conclusive remarks.

2 The lava fountains at Etna in 2021

Etna, one of the most active volcanoes in the world, is a stratovolcano on the east coast of Sicily, Italy. It rises to more than 3,300 m in altitude and has four main summit craters: North-East Crater (NEC), Voragine (VOR), Bocca Nuova (BN) and South-East Crater (SEC). Between February 2021 and October 2021, approximately sixty paroxysmal episodes occurred from the SEC. Of these, 39 episodes lasted several hours and were dispersed towards the E-SE (Calvari et al., 2021). Lava fountains, which are formed by a hot inner core consisting of a mix of liquid clots, pyroclasts, and magmatic gases, are often observed during paroxysmal episodes at Etna and can rise several hundred metres above the volcanic vent (Wilson et al., 1995; Taddeucci et al., 2015). Moreover, during those events it is likely that an eruption column of almost 10-15 km above sea level can form above the lava fountains. Usually, lava fountains are divided in three phases (e.g., Alparone et al., 2003; Mereu et al., 2020; Calvari et al., 2022b): 1) Resumption phase, which commonly begins with slow initial effusion from the vent, followed by a progressive increase in explosive activity; 2) Paroxysmal phase, lasting from 10 to 120 minutes, during which there is a rapid transition from Strombolian activity to sustained lava fountains that rise up an altitude of 2-6 km above the vent; 3) Conclusive phase, during which the eruptive episode gradually ceases.

3 Methods

3.1.1 Sensors and outputs

For the analyses in this work we select all the Etna eruptions characterised by a tephra plume dispersed towards east-southeast flanks of the volcano. These events, listed in Table 1, have been observed using different sensors that are briefly described below:

a) X-band Weather Radar (XWR), located in the airport of Catania, 32 km at SSE Etna summit craters (Figure 1). The scanning agility in elevation and azimuth of this sensor allows it to probe the tephra cloud in any weather condition and both during the day and night (Mereu et al., 2022, 2023; Montopoli, 2016; Vulpiani et al., 2016). Applying the Volcanic Ash

Radar Retrieval (VARR) methodology (e.g. Marzano et al., 2012, 2020; Mereu et al., 2015, 2020) to measure radar reflectivity factor, we estimate: i) the top plume height H_{TP} (km) above sea level, which is the maximum height reached by the eruption column, calculated as the maximum altitude of the radar-detected volume above the volcanic vent contaminated by the minimum detectable tephra concentration; ii) the mass eruption rate Q_M (kg/s), that is estimated by the time-space variation of tephra concentration detected above the Etna summit probing the volcanic plume; iii) the total erupted mass TEM (kg), which is the total mass of pyroclastic material erupted during the explosive event; the ash-fall rate Ra ($kg/m^2 \cdot h$) useful to derive the tephra load integrating this quantity over a time interval and assuming that the radar measurements closer to the ground are indicative of tephra deposited on the ground from the vertical column above a considered position (Mereu et al., 2015).

b) Etna Catania Visible calibrated camera (ECV), located in Catania about 30 km from Etna summit craters (Scollo et al., 2019; Aravena et al., 2023, Figure 1); it allows us to monitor the altitude of dispersed plume during the light hours when the visibility is not compromised by the meteorological cloud cover. In this way, we can derive the time sequence of H_{TP}.

c) Spinning Enhanced Visible and InfraRed Imager (SEVIRI), on board of Meteosat Second Generation (MSG) satellites, is a multispectral radiometer which produces daytime brightness temperature (BT) images with 3 km resolution. Selecting the BT along the Etna summit in the channel of 10.8 μm, that is more sensitive to the tephra dielectric signature, we infer H_{TP} looking for the altitude in which the detected BT can be found in the temperature profile as a function of altitude, which is derived from the hydro-meteorological service of Agenzia Regionale Prevenzione e Ambiente (ARPA) in Emilia Romagna (Scollo et al., 2009; Romeo et al., 2023).

d) Etna Nicolosi Thermal (ENT) infrared camera, located in Nicolosi at about 15 km from Etna summit (Figure 1), which measures the thermal activity associated with lava fountains. It is worth highlighting that when the radar measurements were not available and the volcanic plume was not easily detectable by the satellite sensor or by the visible calibrated camera, analysing the ENT images we have identified the Incandescent Jet Region (IJR), which is a proxy of the lava fountain height. As described in Mereu et al., (2020), the time sequence of maximum height of IJR area can be converted in exit velocity v_{ex}(m/s) of pyroclastic material, using the Bernoulli equation under the following approximations: i) most of the pyroclastic material is sufficiently large to be considered as accelerated projectiles confined in this IJR; ii) atmospheric density variations and drag effects are negligible. Assuming a trustworthy value of tephra-gas mixture density and of surface vent, we can deduce Q_M applying the surface flow approach (SFA) described in Marzano et al., (2020) and Mereu et al., (2022). It is worth noting that H_{TP} obtained from various sensors, such as XWR, ECV, and SEVIRI, exhibits a comparable time trend, as shown in Freret-Lorgeril et al. (2021) and Scollo et al. (2019). The complete ESPs dataset for each of the Etna events considered in this study is displayed in Table 1. Real-time estimation of ESPs can be challenging, especially during the initial phase, increasing the uncertainty in short-term forecasts of plume dispersal (Scollo et al., 2008a). Furthermore, we also collected qualitative information about the eruptions, such as plume height (based on VONA reports; Scollo et al.,

2019; Corradini et al., 2018), the presence of tephra fallout and the start and end times of Strombolian and lava fountain activities (based on bulletins and reports available on the INGV-OE website (www.ct.ingv.it).

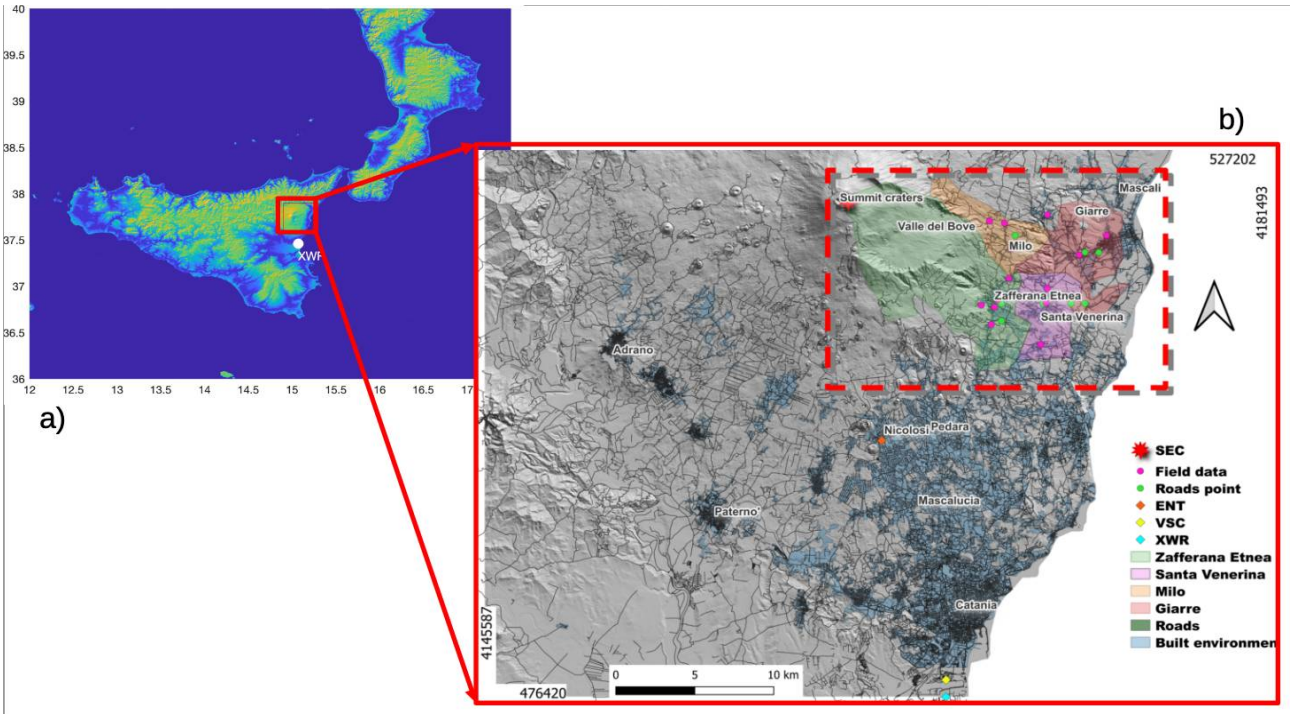

Figure 1: (a) Map of South Italy (Sicily and Calabria), with the red square showing the Etna area framed in the right panel; (b) georeferenced map of road network (dark lines) of the Etna volcano area (shape-files with the road data is publicly available from the Regione Sicilia website: https://www.regione.sicilia.it/). The UTM coordinates (area 33S) are shown in the lower-left part and in the upper-right part of the picture, respectively. The areas of four municipalities, of which three are under examination, and the built environment are highlighted with different colours, whereas each sensor, field data and road points are identified by coloured symbols as listed in the legend in the right side: ground-based sensors employed in this work (the visible camera VSC, the thermal infrared camera ENT and the X-band radar XWR); the South East Carter SEC; 14 field data as derived by Pardini et al. (2021); 8 road points. The rectangle highlighted with the dotted red line identifies the area examined and focused in Figures 3 and 7.

On the other hand, each sensor previously described allows us to measure some features of the lava fountains, which need further elaborations to obtain the ESPs. In this work, H_{TP} (km) and Q_M (kg/s) quantities are directly derived by processing XWR measurements. When it was not possible to determine H_{TP} from XWR, ECV frames or SEVIRI data, we used the ENT images to retrieve the Q_M estimates applying the SFA (Marzano et al. 2020; Mereu et al., 2022). Integrating the SFA in time, we obtain TEM (kg), whereas applying the empirical relation of Mastin et al. (2009), which links Q_M to H_{TP}, we get

the H_{TP} above the Etna summit crater (which is located about 3357 m above sea level). We used the inverse Mastin equation in those cases where the H_{TP} was derived from VSC or SEVIRI imagery to obtain the Q_M time sequence. The starting and ending time for each Etna explosive eruption can be straightly inferred selecting the ends of time range from: i) XWR-based Q_M estimates, where $Q_M > 5\ 10^5$ kg/s; ii) temporal range where ENT camera identifies the lava fountaining feeding the explosive phase; iii) time range in which a quick development of the volcanic cloud is observed by the ECV frames or SEVIRI images. Regarding the wind data, while for Tephra2 simulations we consider a horizontally-constant wind field computed as the mean wind velocity between the Etna summit craters and the maximum value of the H_{TP} sequence, for Fall3D simulations we use the whole meteorological profile. This data, which is used to feed the ash dispersion models, are derived from the European Centre for Medium-Range Weather Forecasts (ECMWF) ERA5 reanalysis (https://www.ecmwf.int/en/forecasts/datasets/reanalysis-datasets/era5). The grain-size distribution usually refers to the volcanic particle size, indicated by the relation $\phi = -\log_2(D)$, where D stands for sphere-equivalent mean diameter (measured in mm). The ϕ refers to the whole deposit, assumed as a Gaussian distribution characterised by a maximum, minimum, mean and standard deviation. In order to consider all possible cases, in this work we vary the median ϕ value between -1 to +1 with a step of 0.5. The georeferenced location and the elevation of the SEC are considered to complete the set of input parameters used, as listed in Table 1. It is worth noting that for each event listed in Table 1, we consider the UTM coordinates of the vent in easting (500024.03 m) and northing (4177699.5 m), or, equivalently, in longitude (15.000273°E) and latitude (37.746592°N), we assume a ϕ with maximum, minimum and standard deviation values equal to -6, 10 and 3, respectively; we repeat each simulation, varying the median ϕ values, so that we obtain a total of 195 simulations from each numerical model.

Table 1. Input parameters used for setting the numerical dispersion model Tephra2 and Fall3D: starting time and ending time of paroxysm (dd:mm:yy, hh:mm), duration Δt (s), top plume height H_{TP} (m) above sea level (a.s.l.) and above volcano vent (a.v.v.), total erupted mass TEM (kg).

START TIME Date T0 UTC	END TIME Date T=T0+Dt UTC	Δt [s]	H_{TP} (a.s.l) [m]	H_{TP} (a.v.v.) [m]	TEM [10^7 kg]
17/02/21 23:40	18/02/21 01:20	6000	9300	5943	18
19/02/21 08:40	19/02/21 10:30	6600	10000	6643	29
28/02/21 07:50	28/02/21 09:50	7200	11900	8543	250
07/03/21 06:20	07/03/21 07:50	5400	11600	8243	110
12/03/21 05:50	12/03/21 10:50	18000	10500	7143	175
14/03/21 23:20	15/03/21 02:20	10800	10957	7600	540

17/03/21 02:50	17/03/21 05:10	8400	6300	2943	22
19/03/21 08:40	19/03/21 10:20	6000	10400	7043	98
19/05/21 03:00	19/05/21 04:30	5400	5000	1643	0.09
22/05/21 20:20	22/05/21 22:40	8400	11057	7700	445
24/05/21 20:30	24/05/21 22:45	8700	11000	7643	468
28/05/21 06:20	28/05/21 07:50	5400	10857	7500	0.4
28/05/21 18:10	28/05/21 21:10	10800	10757	7400	486
30/05/21 03:00	30/05/21 06:00	10800	7500	4143	46.9
02/06/21 08:10	02/06/21 10:50	9600	7600	4243	13.2
04/06/21 16:40	04/06/21 18:40	7200	7500	4143	10
12/06/21 18:30	12/06/21 19:10	2400	9000	5643	17.7
14/06/21 21:40	14/06/21 22:30	3000	6300	2943	56
16/06/21 10:30	16/06/21 13:00	9000	8000	4643	15.8
17/06/21 22:40	17/06/21 23:55	4500	12457	9100	290
20/06/21 22:40	21/06/21 00:40	7200	10900	7543	18
22/06/21 03:30	22/06/21 04:20	3000	8000	4643	11.8
23/06/21 02:00	23/06/21 03:40	6000	7300	3943	77
23/06/21 17:40	23/06/21 19:00	4800	11500	8143	120
24/06/21 09:20	24/06/21 11:00	6000	12200	8843	4.2
25/06/21 18:20	25/06/21 19:40	4800	10664	7307	4.8
25/06/21 00:30	25/06/21 02:40	7800	10616	7259	230
26/06/21 15:20	26/06/21 17:20	7200	9000	5643	22
27/06/21 08:50	27/06/21 10:00	4200	10000	6643	72.9
28/06/21 14:30	28/06/21 15:40	4200	10000	6643	68.8
01/07/21 23:40	02/07/21 01:40	7200	11109	7752	396
04/07/21 15:00	04/07/21 17:50	10200	8200	4843	8.8
06/07/21 22:00	06/07/21 23:45	6300	10000	6643	190
20/07/21 06:20	20/07/21 08:30	7800	11800	8443	79
31/07/21 21:00	31/07/21 23:50	10200	11000	7643	309
09/08/21 02:00	09/08/21 04:40	9600	12000	8643	140
29/08/21 16:40	29/08/21 18:00	4800	9000	5643	13.1
21/09/21 07:30	21/09/21 09:20	6600	10900	7543	47
23/10/21 08:40	23/10/21 11:30	10200	12300	8943	240

3.2 Models

3.2.1 Modelling tephra fallout

In this study, we simulate the transport, dispersal and deposition of tephra with two different numerical Eulerian models: a semi-analytical model Tephra2 and a full computational model Fall3D. We run both models on a grid covering the area (14.5° long, 37° lat) and (16° long, 38.5° lat) with a spatial resolution of ~500 m. Tephra2 allows to evaluate the ground tephra deposition employing the advection-diffusion theory (Bonadonna et al. 2005, 2006; Connor and Connor, 2006; Volentik et al. 2009; Biass et al. 2016, 2017) taking as inputs: H_{TP}; TEM; ϕ; the density of lithics and juveniles (volcanic particles released from the column, which varies widely from ~500 kg/m^3 in highly vesicular clasts to ~2700 kg/m^3 in dense ones); the diffusion coefficient (K), which accounts for atmospheric processes including atmospheric diffusion and cloud gravitational spreading; the fall time threshold (FTT), an empirical threshold that defines the transition between two different laws of atmospheric diffusion and the plume ratio (PR), factor describing the mass distribution in the plume, a horizontally uniform wind field. In the Tephra2 model, it is assumed that a vertical eruption column forms above the vent. The column is discretized, and particles fall from every part of its height. The total tephra mass is vertically distributed within the eruption column according to a probability density function that represents mass as a function of height. The model provides three different mass distributions: uniform, log-normal, and beta distribution. The total grain size distribution for the eruption is estimated assuming a normal distribution in ϕ units (Bonadonna et a., 2005).

Fall3D (v8.0, Folch et al., 2020) models both the particle concentration in the atmosphere (i.e. tephra cloud evolution) and the particle loading at ground level, based on a 3-D time-dependent Eulerian scheme (Costa et al., 2006; Folch et al., 2009; Folch et al., 2012). The model solves the advection-diffusion-sedimentation (ADS) equation over a topographical 3D domain, with several modelling options, including particle aggregation and source terms, among others. The meteorological data used in the simulations are obtained by interpolating the outputs of a meteorological model into the simulation domain. The simulations conducted for this work were performed with no aggregation, using the one-dimensional buoyant plume theory (Folch et al., 2016) as a model for the source term. The meteorological data were retrieved from the ECMWF ERA5-Reanalysis database (Hersbach et al, 2018). This methodology has the potential to track the evolution of particle concentration during an eruption, but the main limitation is the computational cost (Costa et al., 2006). Fall3D uses the same ESP's inputs listed in Table 1, but instead of TEM, it considers Q_M. Figure 2 shows the simulated tephra load (kg/m^2) maps for two among the largest-TEM eruptions (10^8 kg and 10^9 kg), assuming ϕ=0.5. Generally, we note a greater spreading of tephra deposition to the ground simulated by Tephra2 with respect to Fall3D. Both numerical models generate output files in netCDF format (e.g. https://www.unidata.ucar.edu/software/netcdf/) containing geo-referenced data on tephra load (kg/m^2) on the ground in UTM coordinates (zone 33-S for Etna) with a grid spacing of 500 m. The limitations of both models, as a function of variation of input parameters listed in Table 1, as well as and considerations of topography, column

mass distribution models, bulk particle shape, and particle terminal fall velocity, are described in detail in Scollo et al. (2008b).

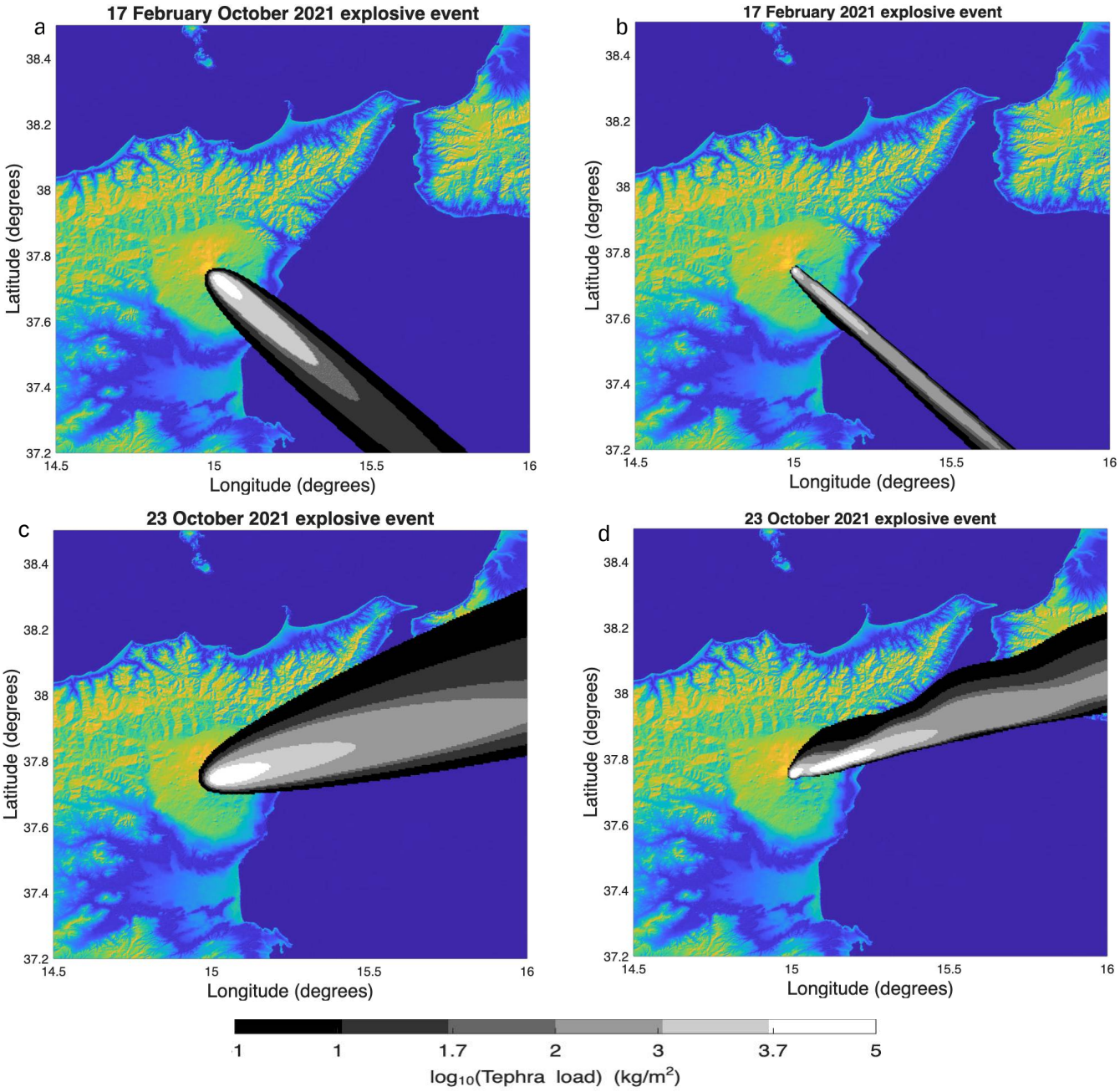

Figure 2: Maps of tephra load (kg/m^2) for the Etna lava fountain event of 17 February 2021 (a)-b)) and of 23 October 2021 (c)-d)), using the Tephra2 (a)-c)) and Fall3D (b)-d)) models. Tephra deposition is plotted as uniform iso-mass contour lines in grayscale, ranging from black for values lower than 10 kg/m^2 to light white for values greater than $5 \cdot 10^3$ kg/m^2.The colour scale is the same in all panels. Global Self-Consistent Hierarchical High-Resolution Geography (GSHHG) map of Matlab.

3.2.2 Calculating the tephra load and mass on the road network

Since our main interest in this work is to calculate the tephra load in the road network, we increase the grid spacing of the tephra load data to 5 m using linear interpolation. Afterwards, we use the Quantum Geographical Information System (QGIS) tool to determine the intersection between the downscaled tephra load data and the areas covered by the road network. While the tracks of road network in the study area is publicly available (geospatial vector data in shapefile format, as shown in Figure 1, from the Regione Sicilia; website https://www.regione.sicilia.it/), an accurate estimate of area of roads is not still available. In order to estimate the area of the roads, we selected several roads in the study area and measured their width using both QGIS integrating an OpenStreetMap layer (https://wiki.openstreetmap.org/wiki/QGIS), and satellite images from GoogleEarth (https://earth.google.com/web/), obtaining an average width of approximately 6 m. Assuming that the roads are generally composed of two carriageways, this value is in agreement with the prescripted widths for urban and extra-urban roads according to the Italian law on roads (art. 2 del Testo Unico, which ranges from 2.8 m and 4 m per carriageway). To consider an uncertainty in this gross measurement, we set the road width to 6 ± 0.5 m. The case study is focused on the road networks located within the municipal area of Milo, Santa Venerina and Zafferana Etnea towns. For a given road segment we calculate the corresponding road area (m^2) and then using the tephra load (kg/m^2) we calculate the total mass (kg) deposited on each road segment. Figure 3 (which covers the area in the rectangle shown with a dotted red line in Figure 1) shows the simulated tephra load (kg/m^2) on the geo-referenced road network within the Milo (light orange area), Santa Venerina (light pink area) and Zafferana Etnea (light green area) municipalities for the event on 28 February 2021.

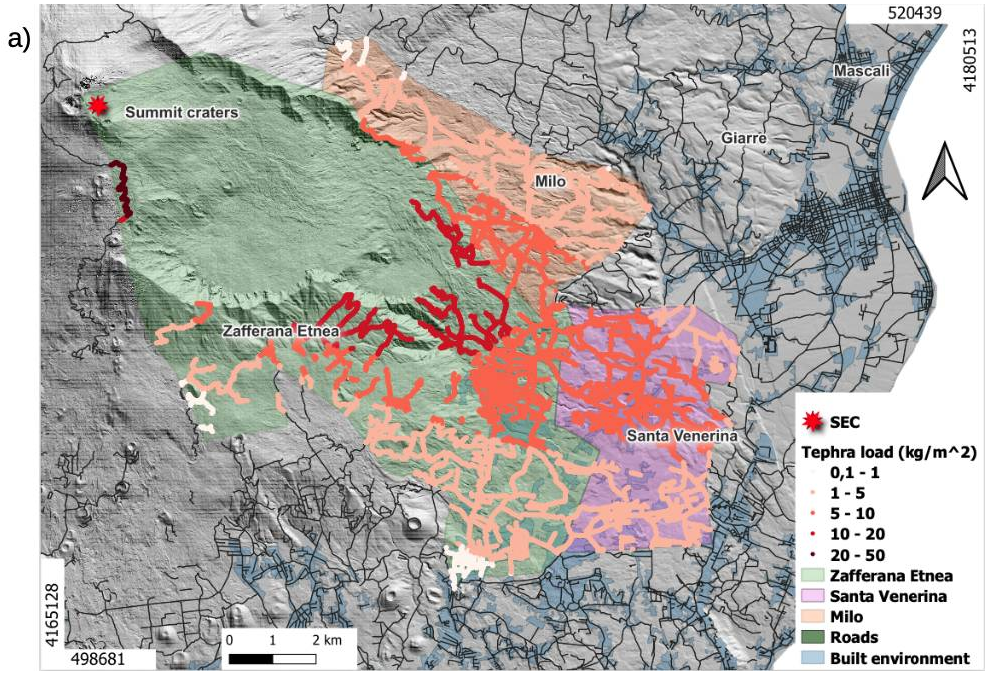

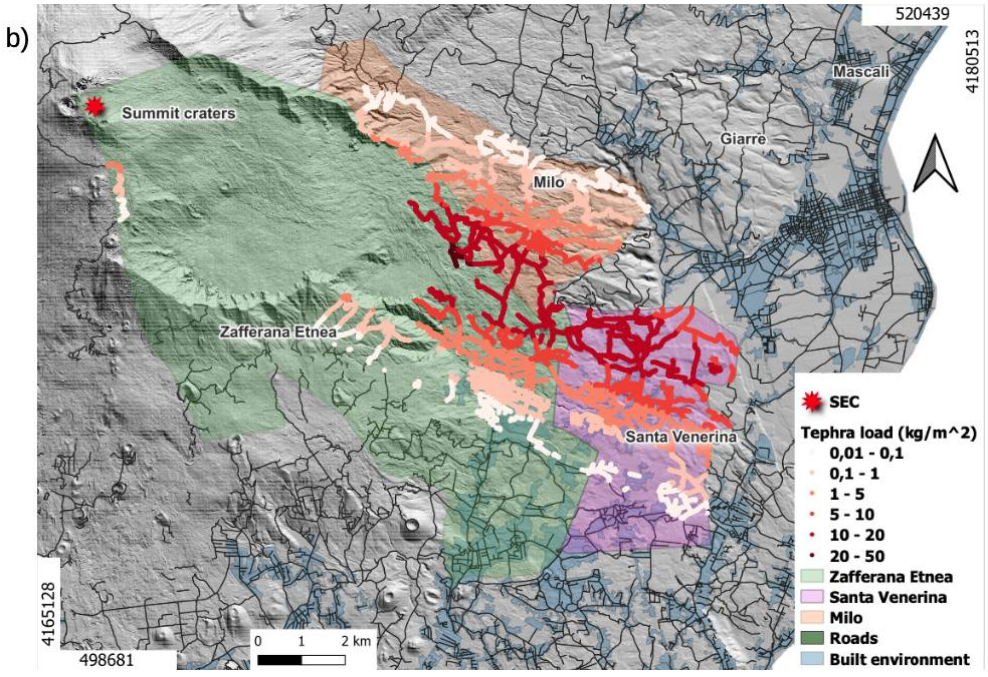

Figure 3: Tephra load (kg/m^2) on the road network of Milo, Santa Venerina and Zafferana Etnea municipalities computed for the Etna explosive event on 28 February 2021, assuming ϕ =0.5 and using both Tephra2 (a) and Fall3D (b) models. The tephra deposits in the road graph are shown in red scale for selected threshold levels of the tephra load values (as shown in

the legend). Georeferenced map of road network (dark lines) of the Etna volcano area (shape-files with the road data is publicly available from the Regione Sicilia website: https://www.regione.sicilia.it/).

4. Results

4.1 Validation: case study on February 28, 2021

In order to verify the results obtained in this study, we focus our attention on the case study of the event on 28 February 2021, which has been observed by the XWR and analysed by Pardini et al. (2021). Table 2 shows the coordinates (longitude, latitude) of 14 points in which field measurements of tephra load are available (from literature, e.g., Pardini et al., 2021) in the selected municipalities (see Figure 1) as well as the results of tephra load derived from the Tephra2 and Fall3D models, fixing the ϕ to 0.5. The XWR retrievals are obtained considering the tephra load rate (kg/m^2 s) related to the first four elevations, which is equal to a few km of altitude with respect to the ground, and integrating it for the whole time sampling of the radar. In this way we can retrieve the tephra load (kg/m^2) related to the whole lava fountain. The correlation between the ground field data (Pardini et al., 2023) and the estimated values using Tephra2, Fall3D, and XWR are plotted, respectively, in Figure 4a, 4b, and 4c. We observe that taking as reference the observed values reported by Pardini et al., 2023, Tephra2 tends to overestimate while Fall3D tends to underestimate the tephra load values. This is evident from the majority of the points dispersed above and below the bisector, as well as from the differences in the slope of the regressive curves with respect to the bisector shown in Figures 4a and 4b. These discrepancies could be due to different dispersal settings used in the numerical model. In contrast, a good correlation between field data and XWR data is observed (Figure 4c), where the points mostly distribute around the bisector and the regressive straight line is almost parallel to it. To evaluate the degree of agreement between filed data and tephra load estimates, we implemented a non-parametric test (namely the Kendall's tau correlation). Table 3 summarises Kendall's tau coefficients, the p-values for testing the null hypothesis of no correlation against the alternative hypothesis of a non-zero correlation; moreover, we estimate the mean absolute percentage error (MAPE) between predicted/estimated data and the observed field data. A Kendall's tau value closer to 1 indicates a better correlation between the field data and the model/estimate data, whereas a low p-value (<1%) indicates a significant correlation. This test confirms that the estimates of both XWR and Tephra2 exhibit a better correlated variation with the field measurements, as indicated by the respective higher tau and lower p-values. The MAPE calculation further supports this conclusion.

Table 2. Etna eruption on February 28, 2021: tephra load (kg/m^2) on 14 sites, each one identified by the latitude and longitude, as deduced by Pardini et al. (2021), and in the same points as derived by Tephra2 and Fall3D models (fixing ϕ =0.5) and retrieved by XWR.

Coordinates (degrees)		Tephra load (kg/m^2)			
Longitude	**Latitude**	**Tephra2**	**Fall3D**	**XWR**	**Field data**
15.102649	37.677930	5.0	0.0	2.4	1.0
15.095485	37.689185	9.0	0.0	4.1	3.3
15.104990	37.688067	8.9	0.2	4.3	3.3
15.107469	37.692398	8.7	1.1	7.6	6.2
15.115397	37.704832	9.1	16.8	8.4	4.7
15.117104	37.722241	4.0	1.9	6.7	4.3
15.112271	37.737129	1.6	0.0	3.5	2.4
15.101504	37.738418	1.6	0.1	3.5	2.1
15.143073	37.742075	0.2	1.7	1.6	0.1
15.165928	37.718516	1.3	0.0	2.3	1.5
15.141991	37.690479	6.4	10.5	3.4	3.9
15.138243	37.666113	4.4	0.0	1.0	1.0
15.142994	37.698936	5.6	13.1	3.1	4.6
15.185512	37.729891	0.2	1.4	0.5	0.5

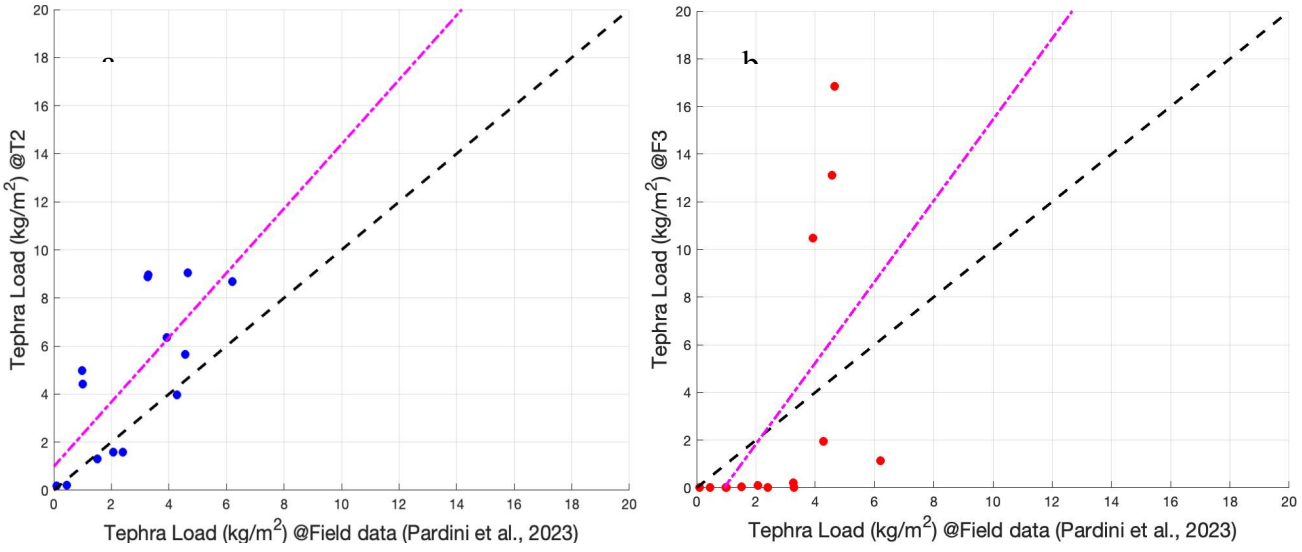

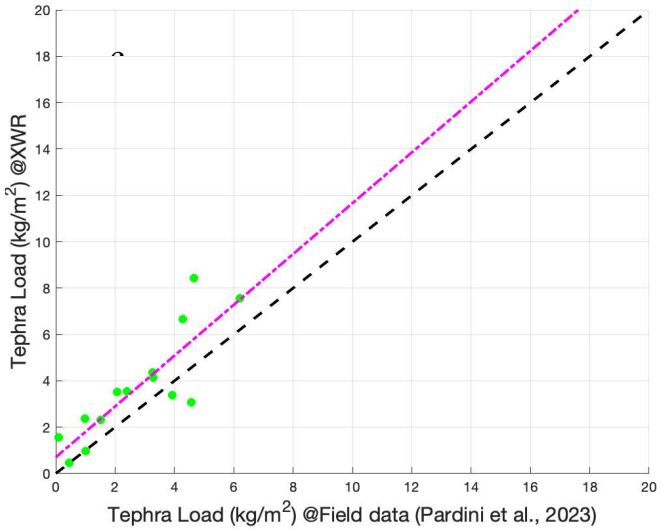

Figure 4: Tephra load correlation: the coloured points represent the field data (Pardini et al., 2023) as a function of the results from Tephra2, Fall 3D and XWR results (blue, red and green dots), as listed in Table 2 and respectively shown in panel a), b), and c). The dashed dark represents the bisector, while the magenta line represents the regressive straight line.

Table 3. Kendall's tau correlation coefficient, p-value, and Mean Absolute Percentage Error (MAPE) computed for the Etna eruption on February 28, 2021

Kendall method	τ	p-value	MAPE
T2-Field data	0.73	$2.8 \cdot 10^{-3}$	48
F3-Field data	0.54	$4.56 \cdot 10^{-2}$	$3.7 \cdot 10^{4}$
XWR-Field data	0.84	$1.3 \cdot 10^{-4}$	34

Assuming the width of (6 ± 0.5) m for each road, we convert the tephra load to tephra mass (kg) for the event of 28 February 2021, assuming $\phi = 0.5$. We selected a few roads, characterised by their larger extension, for each municipality: Via Bellini and Corso Italia in Milo; via Mazzini, via Galimberti and via Stabilimenti in Santa Venerina; via Libertà, via Zafferana Milo and via delle Rose in Zafferana Etnea. We summarise in Table 4 the total tephra mass for streets of Milo, Santa Venerina and Zafferana Etnea as derived from Tephra2 and Fall3D models. The total mass computed for the selected roads in Milo by Tephra2 and Fall3D shows a comparable order of magnitude (10^7 kg), whereas for two selected roads in Zafferana Etnea reveals a disagreement of one order of magnitude. However, the values computed for all municipalities show a maximum variability between approximately five times the tephra deposit collected on the ground (Scollo et al., 2007). The Tephra2 outcomes are generally larger than those of Fall3D, with the ratio between Fall3D and Tephra2 ranging

from 0.3 to 1.4 for the roads and from 0.3 to 1.1 for towns. The variability in road width corresponds to a variability in tephra mass of approximately ± 9 %. The last three rows in Table 4 show the total mass computed on the whole road network of the three municipalities, highlighting the comparable results (same order of magnitude of about 10^9 kg). It is worth noting that the total mass derived from Tephra2 in Zafferana Etnea municipality is four times larger than the total mass derived from Fall3D. This variability can be observed in Figure 3. Not all roads are affected by tephra load, as shown in Figure 3b, and this can be attributed to dissimilarity in the dispersal laws implemented in each model (Scollo et al., 2008; Bonadonna et al., 2005; Folch et al., 2012, 2016). It is important to note that during a typical explosive event at Etna, only a few kilograms of tephra accumulate on a limited number of streets across the three municipalities. This aspect is closely related to the intensity of the explosive event, the amount of pyroclastic material erupted, and the wind dispersal pattern.

Table 4. Total tephra mass (kg) computed on main roads selected of Milo, Santa Venerina and Zafferana Etnea for the Etna eruption on 28 February 2021 as derived from the results obtained using Tephra2 and Fall3D models (fixing ϕ=0.5 and assuming a road width of 6 ± 0.5 m). The total mass on the road network of Milo, Santa Venerina and Zafferana, for three road widths (5.5 m, 6 m, and 6.5 m), is presented in the last three rows. On the right column the mass ratio between Fall3D and Tephra2 results.

Lava fountains on 28 February 2021	**Total tephra mass (10^7 kg)**		
Location	**Tephra2** **(5.5, 6, 6.5 m-width road)**	**Fall3D** **(5.5, 6, 6.5 m-width road)**	**Mass Ratio**
Milo-Via V. Bellini	2.4, 2.6, 2.9	1.3, 1.4, 1.6	0.5
Milo-Corso Italia	1.4, 1.6, 1.7	1.7, 1.9, 2.1	1.2
S. Venerina-Via G. Mazzini	0.02, 0.2, 0.2	0.01, 0.1, 0.1	0.5
S. Venerina-Via D. Galimberti	9.7, 10.6, 11.5	9.8, 10.7, 11.6	1.0
S. Venerina-Via Stabilimenti	0.1, 0.4, 0.5	0.2, 0.8, 1.0	2
Zafferana E.-Via Libertà	2.7, 3.0, 3.2	3.9, 4.3, 4.6	1.4
Zafferana E.-Via Zafferana Milo	1.0, 1.1, 1.2	0.3, 0.3, 0.3	0.3
Zafferana E.-Via delle Rose	1.6, 1.8, 1.9	0.4, 0.5, 0.5	0.3
Total mass on the municipality's road network			
Milo	170.0, 185.4, 209.1	131.4, 143.3, 155.3	0.8
Santa Venerina	129.6, 141.4, 153.2	144.1, 157.2, 170.3	1.1
Zafferana Etnea	659.1, 719.0, 779.0	165.2, 180.2, 195.2	0.3

360 **4.2. Tephra mass on specific road-points**

361 We investigate how the tephra load, derived from both models, can be used to assess the accumulated tephra mass on the
362 road network for the selected municipalities, assuming a cell size of (5×5) metres in the interpolated tephra load map. It is
363 important to highlight that deposited tephra causes disruptions on main roads, specifically in terms of the kilometres of
364 roadways that may face critical driving conditions. The location of the Etna volcano, along with the prevailing westerly and
365 northwesterly winds at high altitude, favours the tephra fallout and dispersal primarily toward east (31%), southeast (35%)
366 and north-west (29%) Etna flanks, and only (6%) directed towards south. These patterns are derived from the analysis of
367 ERA5 reanalysis wind data during 39 eruptive events that occurred in 2021. These results are consistent with the historical
368 statistical distribution of wind direction and relative velocity from the 1990-2007 period at altitudes between 5 and 10 km,
369 as derived from meteorological forecast data (Barsotti et al., 2010; Scollo et al., 2013). The deposited tephra mass, derived
370 from two models, is computed by selecting eight road-points (shown in Figure 1) across different roads in the municipalities
371 of Milo, Santa Venerina (Sven), Zafferana Etnea (Zaff) and Giarre municipalities: provincial roads (SP41, SP92, SP8 and
372 SP59); the highway (E45); and the state road (SS114). To increase the number of road-points on the southeast flank of Etna,
373 we also include road-points from the E45 and SP114 in the municipality of Giarre. In Figure 5 we show the time cumulative
374 tephra mass for different median ϕ values at specific points in the selected roads, as computed by Tephra2 (Figure 5a) and
375 Fall3D (Figure 5b). Generally, increasing the median ϕ increases the deposited tephra mass and vice versa. Obviously, this
376 estimate depends on the collection point, because for a given ϕ, if the mass deposited in the proximal area increases, it
377 decreases in the distal one, since the total mass deposited is conserved. The highest simulated tephra mass values from both
378 models are found at SP59 in Milo, with Tephra2 recording between 2750 and 3375 kg and Fall3D showing between 3000
379 and 4250 kg at the end of the paroxysm sequence. This location is approximately 12 km from the summit of Etna, making it
380 the closest among the analysed points. In contrast, SP92 in Zafferana Etnea shows lower ash loads, with Tephra2 reporting
381 about 725 to 800 kg and Fall3D indicating between 250 and 450 kg at the end of the paroxysm sequence. While Zafferana
382 Etnea is also near Etna (12.2 km away), it is situated further south than Milo. We can evaluate these results taking into
383 account the tolerance boundaries, usually considered as more/less five times the estimated values (Scollo et al., 2007).
384 Indeed, the variability of tephra mass for all the road-points computed with Tephra2 ranges between limit values of 750-
385 3375 kg, whereas the variability derived from Fall3D is between 250-4250 kg. The time-cumulative function derived from
386 Tephra2 presents larger steps in concomitance with events of 14 March, 22 and 28 May, 1 July 2021 for SP59 in Milo, E45,
387 SP49 and SS114 in Santa Venerina and SP8 in Zafferana Etnea whereas E45 and SS114 in Milo show a larger step during
388 the event on 24 May 2021. During the other events, the tephra mass is not large enough to generate major steps in the time-
389 cumulative function. For most road-points, the total accumulated tephra mass stabilises at values between 500 kg and 1250
390 kg after the paroxysm of 20 July 2021, with the exception of SP59 in Milo. The time-cumulative function obtained with
391 Fall3D shows larger steps during the events of 28 May, 2 and 27 June, 31 July 2021 for SP59 in Milo. E45 and SS114 in
392 Milo show a larger step on 27 June 2021, whereas SP41, E45 and SS114 in Santa Venerina exhibit a large step on 29

August 2021, and SP92 in 17 June 2021. In Zafferana Etnea, SP8 shows a time increase of tephra mass, whereas in Zafferana Etnea the tephra mass stabilises at values between 250 kg and 500 kg by the end of June. The time-cumulative tephra mass on SP41, E45 and SS114 in Santa Venerina and SS114 on Milo stabilises between 1325 kg and 2075 kg starting from the beginning of August. Also in the case of Fall3D, SP59 in Milo is confirmed as the most impacted road-point due to accumulation of tephra in time where the time-cumulated tephra increases more than at the other target points, with larger steps, and then stabilises starting from August. These results suggest that, following the 2021 cluster of Etna lava fountains, the roads of Milo and Santa Venerina municipalities have been the most impacted from tephra deposition in time.

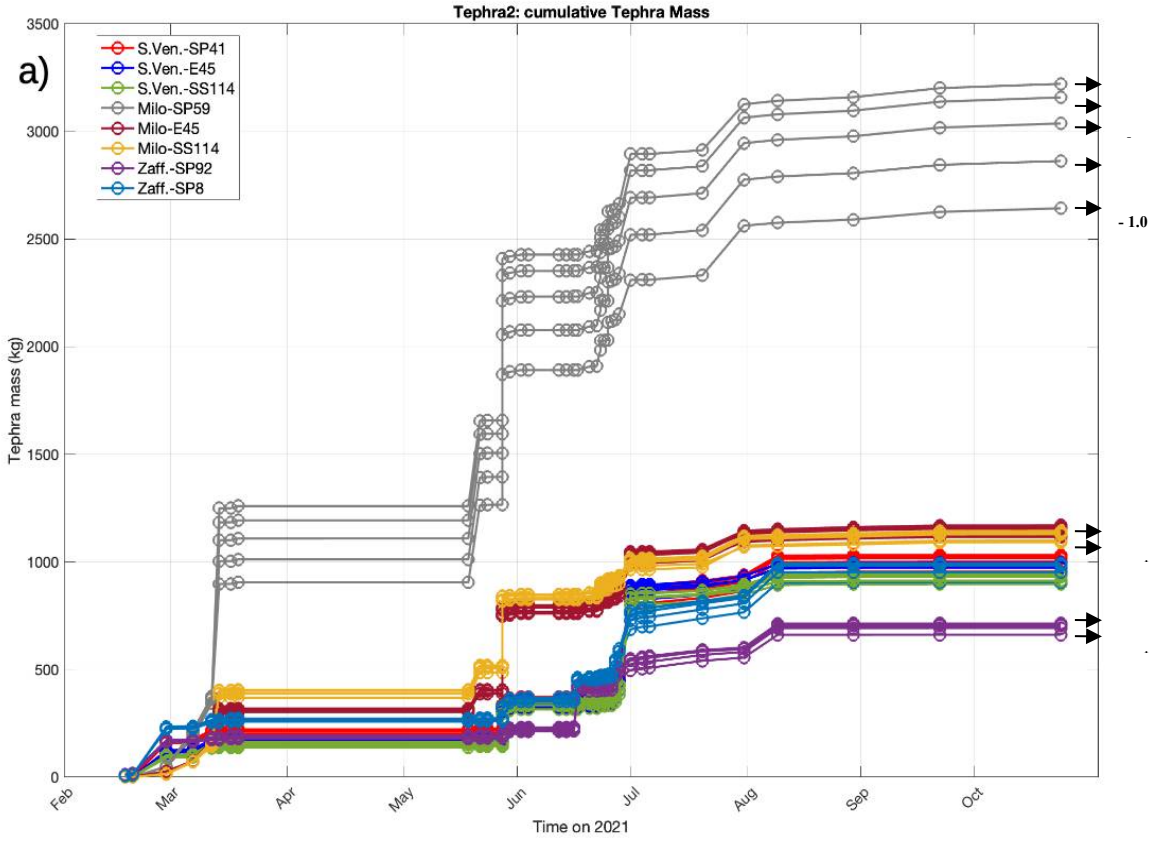

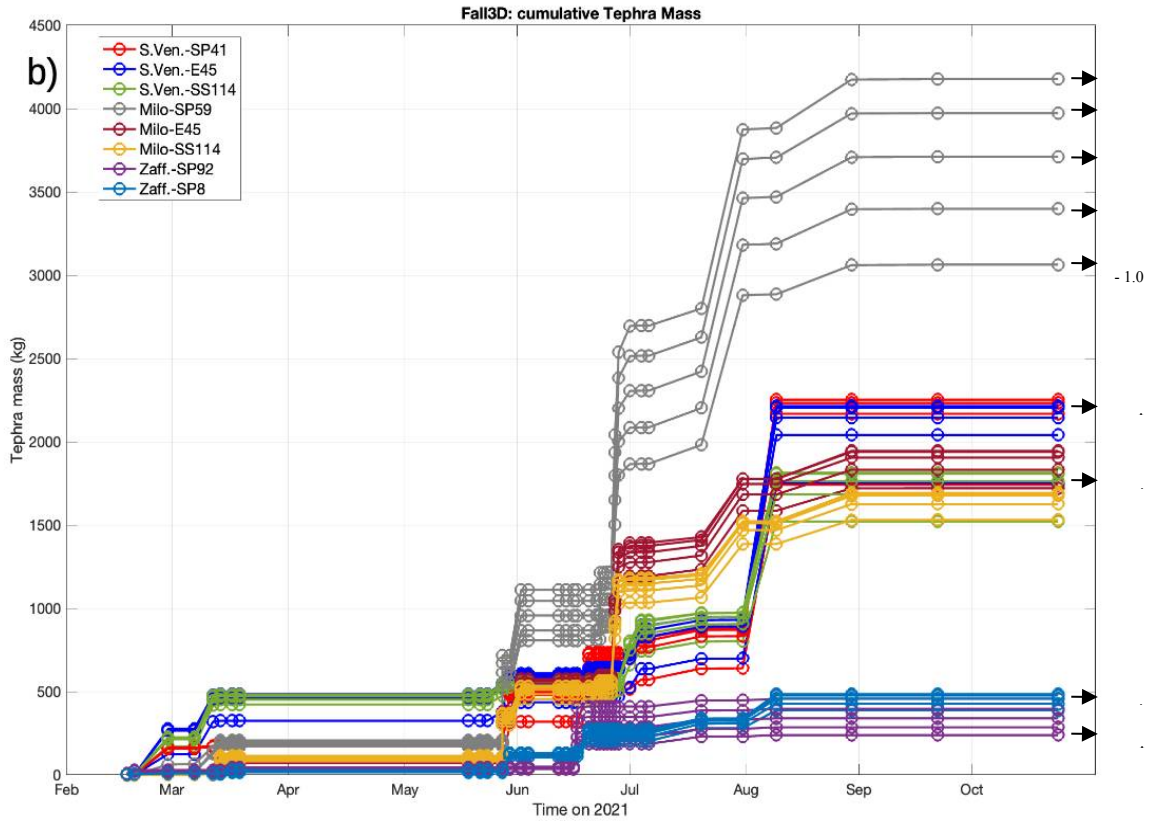

Figure 5: The time series of cumulative tephra mass simulated by the Tephra2 (a) and Fall3D (b) models for all analysed explosive events at Etna in 2021, which shows plumes dispersing to the east and southeast. Each road-point is represented by a unique colour and symbol. We display the cumulative tephra mass corresponding to each road-point and varying the median value of ϕ. The larger the mean grain size, the higher the accumulated load for that road-point, as indicated on the right side of each figure.

4.3 Total mass accumulated on selected roads

In this section we quantify the total tephra mass deposited on selected main roads previously listed in Table 3 for each municipality. Three panels in Figure 6a, 6b and 6c are related, respectively, to the time-cumulative mass on Milo (a), Santa Venerina (b) and Zafferana Etnea (c) computed on selected roads of known area. Analysing the panels in Figure 6 we observe some rapid increases in the cumulative trend of tephra mass mainly for the Fall3D simulations (grey dashed line) with respect to Tephra2 (dark continuous line) simulations. These rapidly increasing trends are found in Milo on 12 March, 28 May (18:10-21:10 UTC), 27 June 2021, in Santa Venerina on 30 May, 17 June 2021 and in Zafferana Etnea. Generally, all the selected roads show a large step in the estimated cumulative tephra mass on 19 February, regardless of the model used. The largest step of total mass is found around June and July, as confirmed by the plots shown in Figure 6a.

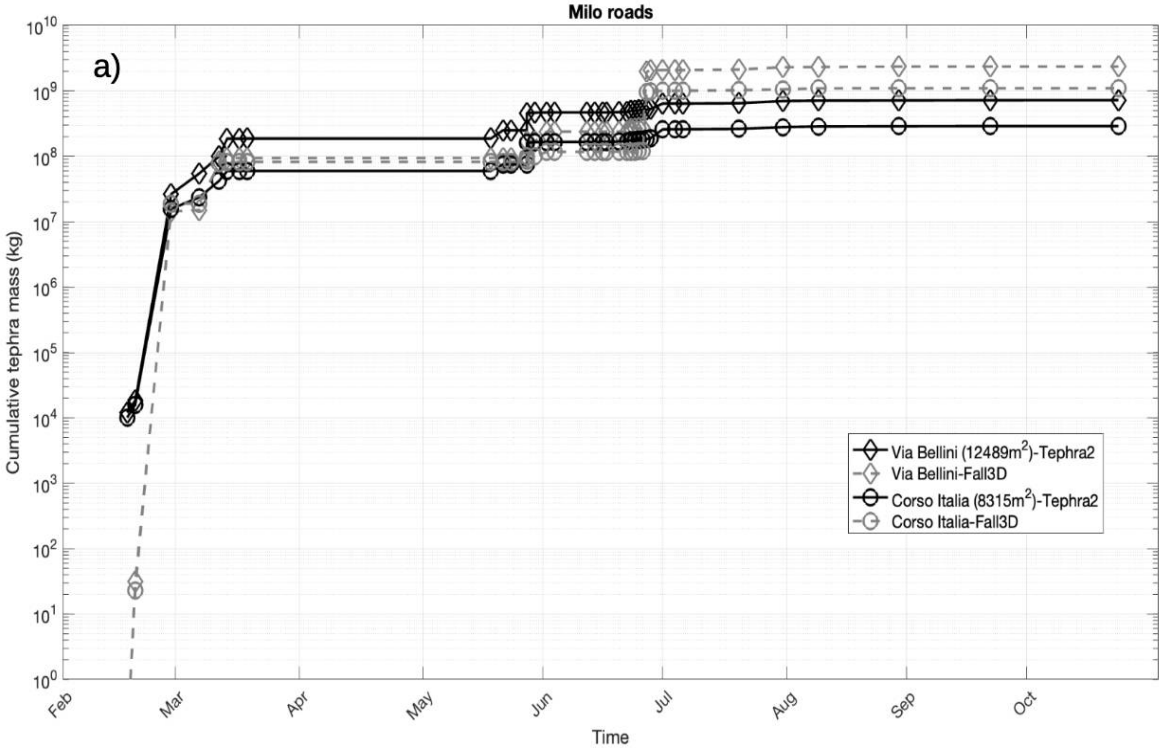
Milo roads
a)
Cumulative tephra mass (kg)
Time
Feb
Mar
Apr
May
Jun
Jul
Aug
Sep
Oct
Via Bellini (12489m^2)-Tephra2
Via Bellini-Fall3D
Corso Italia (8315m^2)-Tephra2
Corso Italia-Fall3D

416

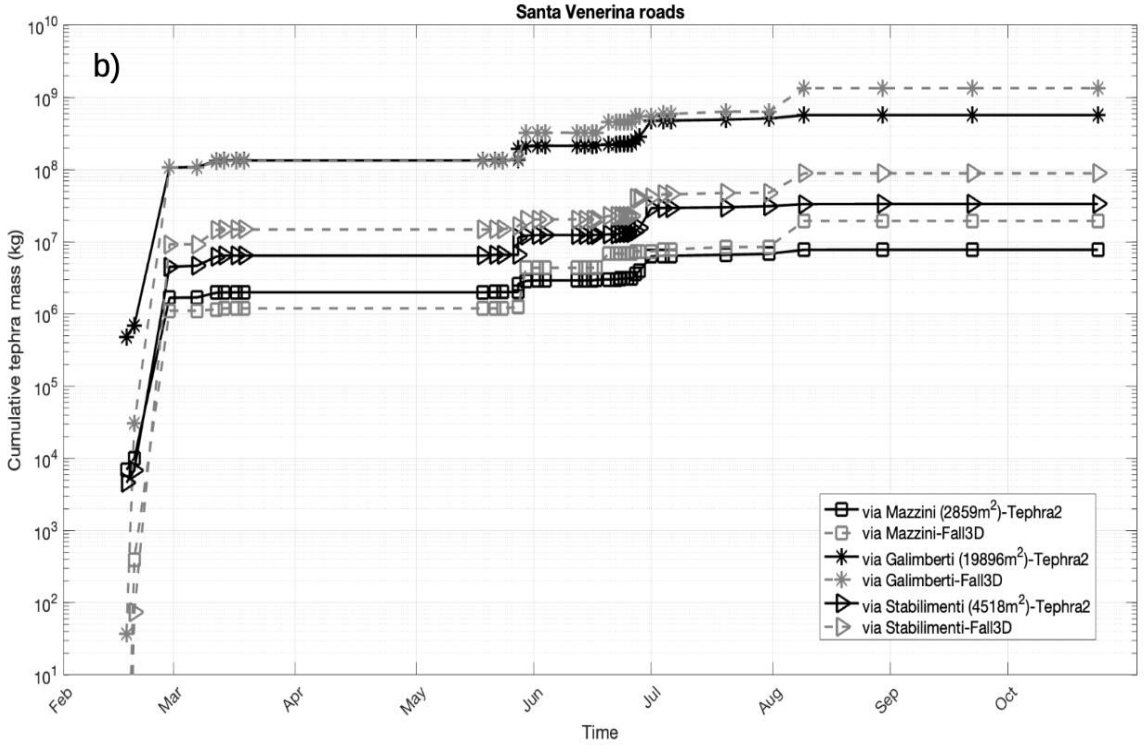
Santa Venerina roads
b)
Cumulative tephra mass (kg)
Time
Feb
Mar
Apr
May
Jun
Jul
Aug
Sep
Oct
via Mazzini (2859m^2)-Tephra2
via Mazzini-Fall3D
via Galimberti (19896m^2)-Tephra2
via Galimberti-Fall3D
via Stabilimenti (4518m^2)-Tephra2
via Stabilimenti-Fall3D

417

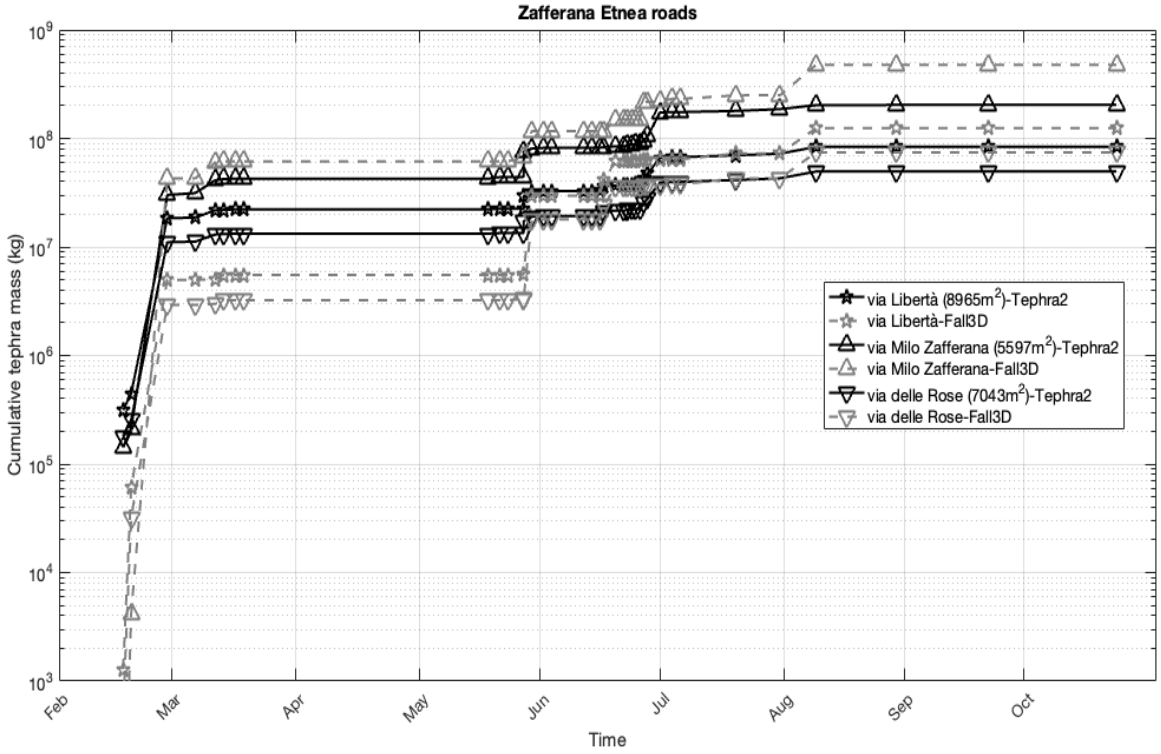

Figure 6: Cumulative tephra mass on selected roads for Milo (a), Santa Venerina (b) and Zafferana Etnea (c), respectively, for all Etna explosive events here analysed and simulated using the Tephra2 (dark continuous line) and Fall3D (grey dashed line) models. Each road is plotted with different symbols and identified by the relative area (m^2, assuming a road width of 6 m), as listed in the legend.

In Table 5 we summarise the total tephra mass deposited during the 39 Etna events in 2021 for the selected roads in each municipality. The last three rows show the total tephra mass computed for the complete road network of each town. The Fall3D estimates are generally larger than those from Tephra2, with the ratio ranging from 1.5 to 3.8 for the roads and from 2.0 to 5.0 for the towns, though the variability can be as much as a factor of five in either direction. We observe that during about one year of Etna's paroxysms, in the nearest municipalities under examination, the estimated value of total tephra mass accumulated in the main streets ranges between 10^6-10^9 kg. A difference of at most one order of magnitude in the total accumulated mass according to the two models is found. It is worth noting that these values are computed under the worst condition, i.e. without considering the tephra mobilisation due to external factors, such as rain or wind, during the complete time range, as well as assuming not road cleaning after each event. Therefore, this tephra mass represents a computed estimate of the total amount of tephra mass that theoretically had to be removed to the roads and disposed of during and after the 2021 crisis.

Table 5. Total mass accumulated over 39 Etna events on the selected roads for Milo, Santa Venerina and Zafferana Etnea municipalities, as simulated by Tephra2 and Fall3D models (fixing ϕ=0.5 and assuming a road width of (6 ± 0.5) m). The total mass on the whole road network of Milo, Santa Venerina and Zafferana, for three road widths (5.5 m, 6 m, 6.5 m), is in the last three rows. On the right column the mass ratio between Fall3D and Tephra2 results.

Location	Mass (10^7 kg)		
	Tephra2 (5.5, 6, 6.5 m-width road)	Fall3D (5.5, 6, 6.5 m-width road)	Mass Ratio
Milo-Via V. Bellini	66.2, 72.2, 78.2	216.3, 235.9, 255.6	3.3
Milo-Corso Italia	26.6, 29.0, 31.3	100.8, 109.9, 119.1	3.8
S. Venerina-Via G. Mazzini	0.09, 0.7, 0.8	0.2, 1.8, 2.1	2.6
S. Venerina-Via D. Galimberti	52.4, 57.0, 61.9	123.7, 134.6, 146.2	2.4
S. Venerina-Via Stabilimenti	0.8, 3.1, 3.6	2.0, 8.2, 9.7	2.6
Zafferana E.-Via Libertà	7.7, 8.4, 9.1	11.4, 12.4, 13.5	1.5
Zafferana E.-Via Zafferana Milo	18.7, 20.4, 22.1	43.7, 47.7, 51.7	2.4
Zafferana E.-Via delle Rose	4.6, 5.0, 5.4	6.8, 7.4, 8.1	1.5
Total mass on the whole road network of each municipality			
Milo	7310.7, 7975.3, 8639.9	14937.5, 16295.5, 17653.5	2.0
Santa Venerina	488.4, 805.5, 952.0	1510.4, 2641.9, 3122.3	3.3
Zafferana Etnea	5162.3, 5631.5, 6100.9	26632.4, 29053.5, 31474.6	5.0

4.4 Total mass accumulated on the full road network

Similarly to Figure 3, Figure 7 shows the cumulative tephra load (kg/m^2) on the geo-referenced road map within the Milo (light orange area), Santa Venerina (light pink area) and Zafferana Etnea (light green area) municipalities for all 39 Etna lava fountains, computed using Tephra2 (Figure 7.a)) and Fall3D (Figure 7.b)) models.

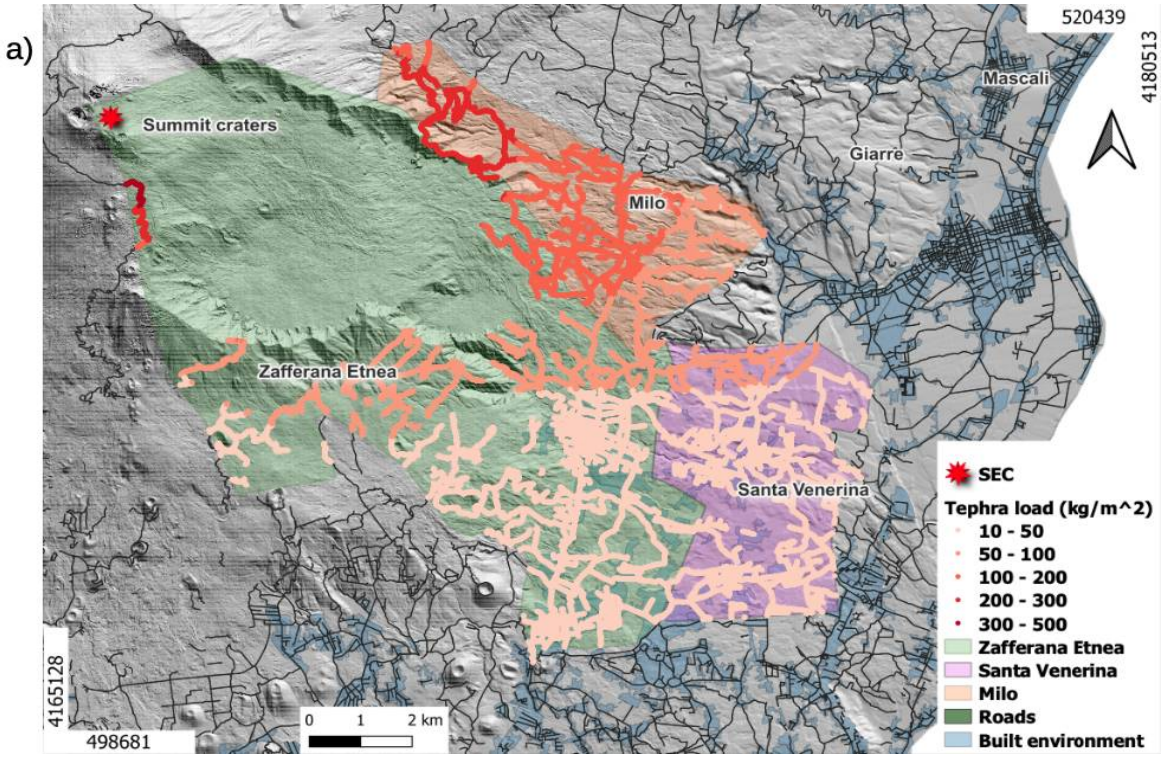
a)
520439
4180513
Mascali
Giarre
Milo
Summit craters
Zafferana Etnea
Santa Venerina
SEC
Tephra load (kg/m^2)
10 - 50
50 - 100
100 - 200
200 - 300
300 - 500
Zafferana Etnea
Santa Venerina
Milo
Roads
Built environment
4165128
498681
0 1 2 km

447

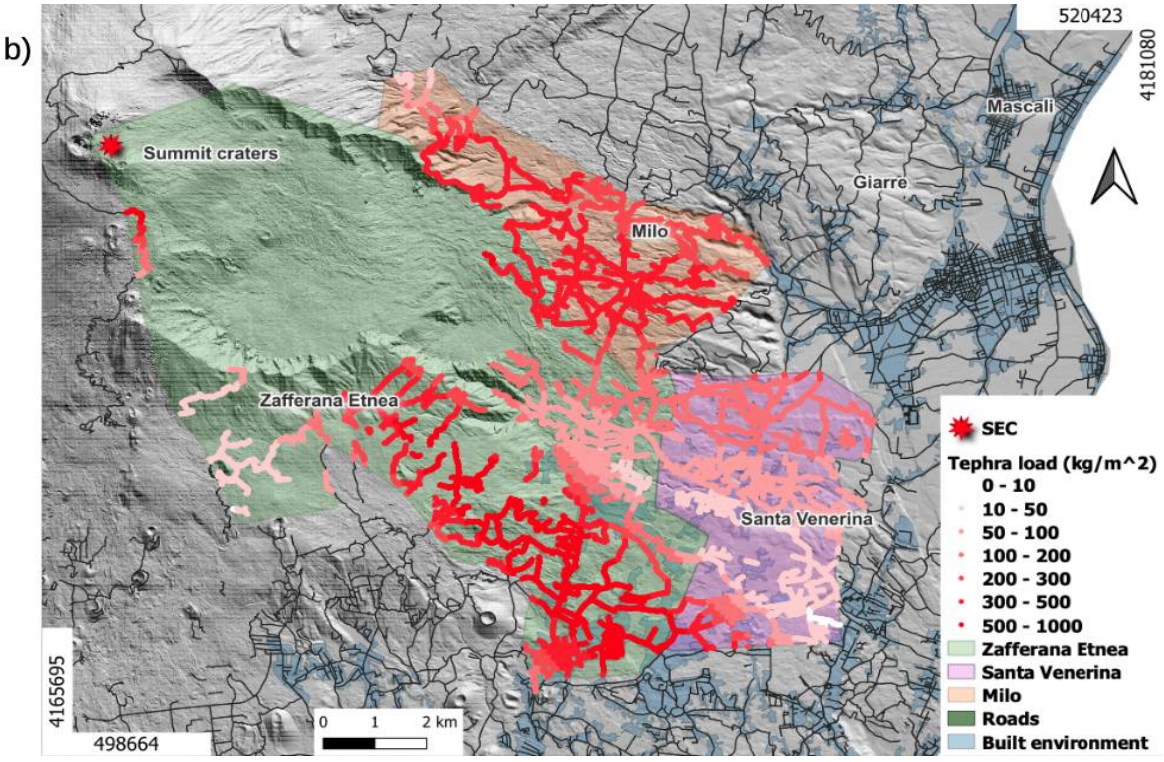
b)
520423
4181080
Mascali
Giarre
Milo
Summit craters
Zafferana Etnea
Santa Venerina
SEC
Tephra load (kg/m^2)
0 - 10
10 - 50
50 - 100
100 - 200
200 - 300
300 - 500
500 - 1000
Zafferana Etnea
Santa Venerina
Milo
Roads
Built environment
4165695
498664
0 1 2 km

448

Figure 7: Cumulative tephra load (kg/m2) for all 39 Etna lava fountains analysed in this work, computed on the whole road network of Milo, Santa Venerina and Zafferana Etnea using (a) Tephra2 and (b) Fall3D models, assuming ϕ=0.5. The road graph is bold highlighted and in red scale coloured in function of deposited tephra values. Georeferenced maps of road network (dark lines) of the Etna volcano area (shape-files with the road data is publicly available from the Regione Sicilia website: https://www.regione.sicilia.it/).

Considering the area of each road, we compute the time-cumulative tephra mass (kg) relative to Milo, Santa Venerina and Zafferana, over the whole road network, as computed by both numerical models (Figure 8). Normally, the cumulative tephra mass derived from Tephra2 (dark continuous line) after an initial rapid growth tends to stabilise, in contrast with the trends obtained using Fall3D (grey dashed line), which present rapid increases in estimates throughout the sequence. These leaps in Milo are for the events on 28 May, 23 June (17:40-19:00 UTC) and 27 June 2021, in Santa Venerina on 28 February, 23 and 27 June 2021, and in Zafferana Etnea on 28 February and 17 June 2021. The maximum value of tephra mass deposited on the whole road network in the three municipalities ranges between 10^{10} to 10^{12} kg.

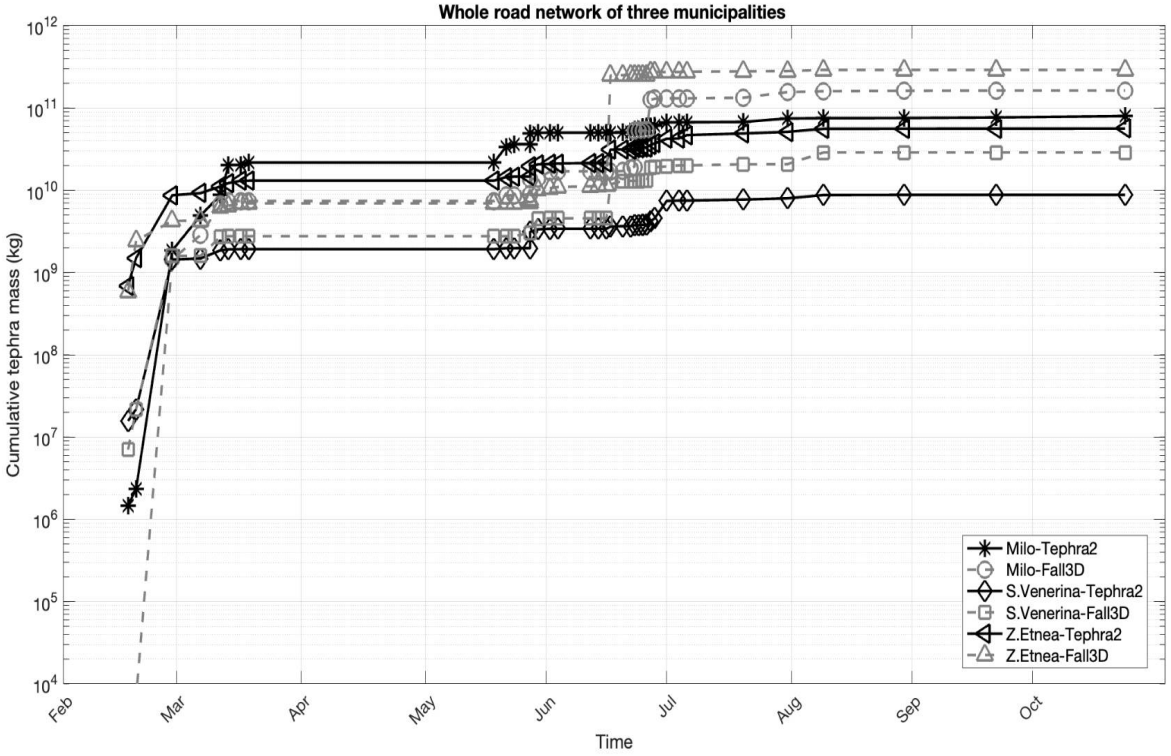

Figure 8: Cumulative tephra mass for all the 2021 Etna lava fountains analysed in this work, simulated using Tephra2 (dark continuous line) and Fall3D (grey dashed line) models, for the whole road network in Milo, Santa Venerina and Zafferana Etnea.

4.5. Analysis of variability in tephra mass results

The estimates of tephra mass, as a function of uncertainty variation related to ESPs used as input to train both numerical models and the specific limitations of the two dispersal models, are already well-documented in the literature (Scollo et al., 2008b). In the present work, we evaluated the potential mass load and total mass accumulated on the road networks of several target towns. Due to the complexity of the Fall3D model, requiring significant computational resources compared to Tephra2, the number of simulations considered for each analysed eruption was limited to the GSD variability. However, the comparison between the results provided by the two models allows a first analysis of the variability in tephra mass estimates. The evaluation of the results for the case study on 28 February 2021, observed by the XWR and analysed by Pardini et al. (2021), allowed us to confirm Tephra2 as a useful numerical model for rapid assessment of tephra dispersal and deposition on road points, and for quickly evaluating the relative tephra fallout hazard. These results are consistent with the distribution of field data in relation to XWR measurements and model outcomes shown in Figure 4a, 4b, and 4c. The Kendall's tau correlation coefficient and the MAPE presented in Table 4 further support our findings. We also highlight the high performance of XWR in measuring these quantities, although these observations are not always available in real-time. By shifting focus from individual road points to selected roads for the same Etna eruption event on 28 February 2021, we observe that the Fall3D estimates are approximately comparable with those of Tephra2, as confirmed by a ratio ranging from 0.3 to 2. When considering the entire sequence of 39 Etna eruptive events, Fall3D estimates are higher than Tephra2 for the main roads in the three municipalities and for the entire road network selected in this work. Furthermore, assuming a variability of road width (±0.5 m) in our computations, we estimate a variability in tephra mass of approximately ± 9%. All of this information allows us to outline a more comprehensive framework for estimating the mass of tephra accumulated on roads, which is essential for managing the impact of volcanic eruptions.

5. Discussion and conclusions

Considering the question about the quantification of the total tephra mass deposited in a given infrastructure of interest following an (or a series of) explosive volcanic eruption(s), in this work we assessed, for the first time, the cumulated tephra mass on the road networks in three selected towns on Etna's eastern flank during several paroxysms that occurred in 2021. This accumulated mass is a theoretical estimate of the amount of material that had to be removed from the roads and disposed of during the 2021 volcanic activity. We have focussed on three target municipalities located on the east flank, i.e. Milo, Santa Venerina and Zafferana Etnea. According to the law at the time of the eruption, such material had to be handled and disposed of as special waste (Art. 35 decreto legge 77/2021). At the time of writing this paper a new law allows the use of this material for other purposes (DA n.8/Gab. 22/04/2024, https://www.regione.sicilia.it) as, for example, building construction. Processing measurements derived from visible and thermal cameras of INGV-OE, and, when available, from SEVIRI images and the XWR data, we can retrieve the main ESPs, useful inputs to run numerical models. In this way we

can simulate and evaluate the cumulated tephra load on roads in time. Processing these results with the QGIS tool, we are able to identify the roads more exposed to tephra deposition. We consider that the results of this analysis can be a valuable source of information to support the management of volcanic crises and for planning the reinstatement of road networks after a crisis.

It is known that effective and realistic transport management strategies are essential into volcanic contingency planning in sectors where key infrastructure are at risk, such as the road networks. Evaluating tephra mass using two (or more) different models allows assessing epistemic uncertainty, to estimate the different sensitivity of each model to same input ESPs and the variability of the median ϕ. It is worth highlighting that in this work, we have neglected the uncertainties in the ESP values (such as Q_M, TEM and H_{TP}), but this analysis is already available in literature (see e.g., Scollo et al., 2008b). However, these values are affected by various sources of uncertainty, including pre- and post-processing of data, as well as instrument sensitivity and accuracy, all of which can significantly impact the model outputs (see e.g., Mereu et al, 2023). This can lead to larger uncertainties in the simulated tephra load in addition to those related to the different model settings and the physical assumptions implemented in each numerical model.

In this work we are not considering the effect of rain which can remain trapped in the tephra deposit. Furthermore, depending on the rain's intensity, the road traffic safety can worsen (e.g., by making the transport network particularly slippery) or can be improved (e.g., by washing the road surface from the ash deposit). Specific thresholds of tephra load that can damage the main roads system, and the necessary actions to mitigate the tephra effects are defined and known in the literature (e.g. Jenkins et al. 2015; Bonadonna et al. 2021b; Table 8 in Bonadonna et al., 2021a).

As a final consideration, we point out the importance of the validation of the results of tephra load simulation obtained with two different numerical models by comparing their output with ground sampling data (in our case available from Pardini et al., 2023) as well as with the XWR retrievals for the Etna explosive activity on February 28, 2021. The tephra deposit estimations, as listed in Tables 2 and 3, highlight the good agreement among the ground sampling, XWR retrievals and the output of numerical models. This observation makes us confident to use the two different models in evaluating not only qualitatively but also quantitatively the tephra deposited during recent Etna paroxysms. In this way it is possible to provide plausible values of ground cumulated tephra mass on roads, and identify which routes in the road network of the target towns may be most impacted in next eruptions.

We consider that the analyses and the results proposed in this paper provide interesting inputs for supporting decision making and crisis management. Indeed, such analyses may support planning for clean-up following volcanic eruptions, which is essential for effective volcanic risk management (Hayes et al., 2019). Post-eruption clean-up of tephra deposits on roads is a widespread and costly activity, both in terms of time and resources, and frequently it is an unplanned activity (Hayes et al., 2019). Combining different cleaning methods, such as sweeping, suction, spraying and air blasting, could help speed up tephra fallout removal from high-priority roads used in the management of these events, especially before markings are fully covered (with thickness ranging from 1 to 10 mm), in order to ensure safety during cleaning operations.

Understanding the economic impact on affected areas (Hayes et al., 2015; Magill et al., 2006) also contributes to better risk management. Geospatial analysis methods are well-documented in the literature for estimating the duration of roads cleaning-up (Hayes et al., 2017), although these operations are influenced by complex interactions between physical factors (e.g. erupted volume, column height, grain-size, wind speed and direction, and rainfall) and social factors (e.g. social priorities, prior planning, previous experience, and infrastructure interdependencies) (Hayes et al., 2015). Moreover, the presented results may support decision makers in different ways e.g. for planning and consequently for better management of a future volcanic crisis due to explosive activity of Etna volcano, as well as for getting valuable information about the order of magnitude of the total mass of tephra available for preparing the subsequent disposal and/or reuse.

Acknowledgments: This work was performed in the framework of the INGV Project "Pianeta Dinamico" (D53J19000170001), funded by MUR ("Ministero dell'Università e della Ricerca, Fondo finalizzato al rilancio degli investimenti delle amministrazioni centrali dello Stato e allo sviluppo del Paese, legge 145/2018"). Fall3D simulations have been performed thanks to the computational resources of the ADA cluster of Istituto Nazionale di Geofisica e Vulcanologia, Sezione di Bologna. Manuel Stocchi was funded by the "PNIR - Programma Nazionale Infrastrutture di Ricerca" with the CIR01_00013 project. C. Bonadonna was funded by SNSF project #200021_188757.

References

Ágústsdóttir, A. M.: Ecosystem approach for natural hazard mitigation of volcanic tephra in Iceland: building resilience and sustainability. Nat. Hazards 78, 1669–1691. doi: 10.1007/s11069-015-1795-6, 2015.

Alparone, S., Andronico, D., Lodato, L., and Sgroi, T.: Relationship between tremor and volcanic activity during the Southeast Crater eruption on Mount Etna in early 2000, J. Geophys. Res., 108 (B5), 2241, doi:10.1029/2002JB001866, 2003.

Andronico, D.; Cannata, A.; Di Grazia, G.; Ferrari, F.: The 1986–2021 paroxysmal episodes at the summit craters of Mt. Etna: Insights into volcano dynamics and hazard. Earth-Sci. Rev., 220, 103686, 2021.

Aravena, A., Carparelli, G., Cioni, R., Prestifilippo, M., & Scollo, S.: Toward a real-time analysis of column height by visible cameras: an example from mt. Etna, in Italy. Remote Sensing, 15(10), 2595, 2023.

S. Barsotti, S., Andronico, D., Neri, A. Del Carlo, P., Baxter, P.J.,W.P. Aspinall, W.P., Hincks, T.: Quantitative assessment of volcanic ash hazards for health and infrastructure at Mt. Etna (Italy) by numerical simulation. Journal of Volcanology and Geothermal Research 192, 85–96, 2010.

Barsotti, S., Di Rienzo, D.I., Thordarson, T., Björnsson, B.B. and Karlsdóttir S.: Assessing Impact to Infrastructures Due to Tephra Fallout From Öræfajökull Volcano (Iceland) by Using a Scenario-Based Approach and a Numerical Model, Front. Earth Sci. 6:196, doi: 10.3389/feart.2018.00196, 2018.

Baxter., P.: Medical effects of volcanic eruptions. Bull. Volcanology, 52, 532, doi: 10.1007/BF00301534, 1990.

Bebbington, M., Cronin, S. J., Chapman, I., and Turnera, M. B.: Quantifying volcanic ash fall hazard to electricity infrastructure. J. Volcanol. Geother. Res. 177:4, doi: 10.1016/j.jvolgeores.2008.07.023, 2008.

Biass S., Bonadonna C., Traglia F. et al: Probabilistic evaluation of the physical impact of future tephra fallout events for the Island of Vulcano, Italy. Bull Volcanol 78:1–22, https://doi.org/10.1007/ s00445-016-1028-1, 2016.

Biass, S., Todde A., Cioni R., Pistolesi M., Geshi N., Bonadonna C.: Potential impacts of tephra fallout from a large-scale explosive eruption at Sakurajima volcano, Japan, Bull Volcanol 79:73 DOI 10.1007/s00445-017-1153-5, 2017.

Blake, D.M.; Wilson, T.M.; Gomez, C.: Road marking coverage by volcanic ash. Environ. Earth Sci. 75, 1–12, 2016.

Blake, D. M., Wilson T. M., Cole J. W., Deligne N. I. and Lindsay, J. M.: Impact of Volcanic Ash on Road and Airfield Surface Skid Resistance, Sustainability 2017, 9, 1389, doi: 10.3390/su9081389, 2017.

Blong, R.J. Volcanic Hazards: A Sourcebook on the Effects of Eruptions; Academic Press Inc.: Sydney, Australia, 1984.

Blong, R. J.: Volcanic hazards risk assessment, Monitoring and Mitigation of Volcano Hazards, eds R. Scarpa and R. I. Tilling (Berlin: Springer), 1996.

Bonadonna, C., C. B. Connor, B. F. Houghton, L. Connor, M. Byrne, A. Laing, and T. K. Hincks: Probabilistic modeling of tephra dispersal: Hazard assessment of a multiphase rhyolitic eruption at Tarawera, New Zealand, J. Geophys. Res., 110, B03203, doi:10.1029/2003JB002896, 2005.

Bonadonna, C.: Probabilistic modelling of tephra dispersal, in: Statistics in Volcanology, edited by: Mader, H., Cole, S., and Connor, C. B., IAVCEI Series, Volume 1, Geological Society of London, 2006.

Bonadonna C, Frischknecht C, Menoni S, Romerio F, Gregg CE, Rosi M, Biass S, Asgary A, Pistolesi M, Guobadia D., Gattuso A., Ricciardi A, Cristiani C.: Integrating hazard, exposure, vulnerability and resilience for risk and emergency management in a volcanic context: the ADVISE model, Journal of Applied Volcanology, https://doi.org/10.1186/s13617-021-00108-5, 2021a.

Bonadonna C, Biass S, Menoni S, Chris EG: Assessment of risk associated with tephra-related hazards, In: Papale, P (Ed.), Forecasting and Planning for Volcanic Hazards, Risks, and Disasters: Elsevier, 329-378. (Hazards and Disasters), 2021b.

Calvari, S.; Cannavò, F.; Bonaccorso, A.; Spampinato, L.; Pellegrino, A.G.: Paroxysmal Explosions, Lava Fountains and Ash Plumes at Etna Volcano: Eruptive Processes and Hazard Implications. Front. Earth Sci. 6, 107, https://doi.org/10.3389/feart.2018.0010.7, 2018.

Calvari, S., Bonaccorso, A., Ganci, G.: Anatomy of a Paroxysmal Lava Fountain at Etna Volcano: The Case of the 12 March 2021, Episode. RemoteSensing,13,3052. https:// doi.org/10.3390/rs13153052, 2021.

Calvari, S.; Biale, E.; Bonaccorso, A.; Cannata, A.; Carleo, L.; Currenti, G.; Di Grazia, G.; Ganci, G.; Iozzia, A.; Pecora, E.; et al.: Explosive Paroxysmal Events at Etna Volcano of Different Magnitude and Intensity Explored through a Multidisciplinary Monitoring System. Remote Sens., 14, 4006, https://doi.org/10.3390/rs14164006, 2022(a).

Calvari, S.; Nunnari, G.: Comparison between Automated and Manual Detection of Lava Fountains from Fixed Monitoring Thermal Cameras at Etna Volcano, Italy. Remote Sens., 14, 2392. https://doi.org/10.3390/rs14102392, 2022 (b).

Casadevall, T. J.: The 1989–1990 eruption of redoubt volcano, Alaska: impacts on aircraft operations, J. Volcanol. Geother. Res. 62, 301–316. doi: 10.1016/0377- 0273(94)90038- 8, 1994.

Connor, L. G. and Connor, C. B.: Inversion is the key to dispersion: Understanding eruption dynamics by inverting tephra fallout, in: Statistics in Volcanology, Society for Industrial and Applied Mathematics, Special Publication of IAVCEI N. 1, Mader, H., Cole, S., and Connor, C. B., 231–242, Geological Society, London, 2006.

Corradini, S., Guerrieri, L., Lombardo, V., Merucci, L., Musacchio, M., Prestifilippo, M., Scollo, S., Silvestri, M., Spata, G., Stelitano, D.: Proximal monitoring of the 2011-2015 Etna lava fountains using MSG-SEVIRI data. Geosciences 8, 140, 2018.

Costa A., G. Macedonio a, A. Folch: A three-dimensional Eulerian model for transport and deposition of volcanic ashes, Earth and Planetary Science Letters 241, 634–647, 2006.

Costa, A., Folch, A., Macedonio, G., Giaccio, B., Isaia, R., and Smith, V. C.: Quantifying volcanic ash dispersal and impact of the Campanian Ignimbrite super-eruption, Geophysical Research Letters, 39, https: //doi.org/10.1029/2012GL051605, 2012.

Dominguez, L., Bonadonna, C., Frischknecht, C., Menoni, S. and Garcia, A.: Integrative Post-event Impact Assessment Framework for Volcanic Eruptions: A Disaster Forensic Investigation of the 2011–2012 Eruption of the Cordón Caulle Volcano (Chile). Front. Earth Sci. 9:645945. doi: 10.3389/feart.2021.645945, 2021.

Freret-Lorgeril, V., Bonadonna, C., Corradini, S., Donnadieu, F., Guerrieri, L., Lacanna, G., Marzano, F.S., Mereu, L., Merucci, L., Ripepe, M., et al.,: Examples of Multi-Sensor Determination of Eruptive Source Parameters of Explosive Events at Mount Etna. RemoteSensing, 13, 2097. https:// doi.org/10.3390/rs13112097, 2021.

Folch, A., Costa A, Macedonio G.: FALL3D: A computational model for transport and deposition of volcanic ash. Computers and Geosciences 35, 1334–1342, 2009.

Folch, A., Costa, A, Basart, S.: Validation of the FALL3D ash dispersion model using observations of the 2010 Eyjafjallajökull volcanic ash clouds, Atmospheric environment volume 48, Pages 165-183, 2012.

Folch, A., Costa, A., and Macedonio, G.: FPLUME-1.0: An integral volcanic plume model accounting for ash aggregation, Geosci. Model Dev., 9, 431–450, https://doi.org/10.5194/gmd-9-, 2016.

Folch, A., Mingari, L., Gutierrez, N., Hanzich, M., Macedonio, G. and Costa, A.: FALL3D-8.0: a computational model for atmospheric transport and deposition of particles, aerosols and radionuclides – Part 1: Model physics and numerics, https://doi.org/10.5194/gmd-13-1431, 2020.

Gordon, K.D.; Cole, J.W.; Rosenberg, M.D.; Johnston, D.M.: Effects of volcanic ash on computers and electronic equipment. Nat. Hazards, 34, 231–262, 2005.

625 Guffanti, M., Mayberry, G. C., and Casadevall, T. J.: Volcanic hazards to airports. Nat. Hazards 51, 287–302. doi:
626 10.1007/s11069-008-9254-2, 2009.
627 Hayes, J. L., Wilson, T. M. and Magill, C.: Tephra fall clean-up in urban environments, Journal of Volcanology and
628 Geothermal Research 304, 359–377, 2015.
629 Hayes, J., Wilson, T.M., Deligne, N.I., Cole, J., Hughes, M.: A model to assess tephra clean-up requirements in urban
630 environments. J. Appl. Volcanology, 6:1. https://doi.org/10.1186/s13617-016-0052-3, 2017.
631 Hayes, J. L., Wilson, T. M., Carol Stewart, C., Villarosa, G., Salgado, P., Beigt, D., Outes, V., Deligne, N. I., and
632 Leonard, G. S.: Tephra clean-up after the 2015 eruption of Calbuco volcano, Chile: a quantitative geospatial assessment in
633 four communities, Journal of Applied Volcanology, 8:7 https://doi.org/10.1186/s13617-019-0087-3, 2019.
634 Hayes, J.L., Biass, S., Jenkins, S.F. et al. Integrating criticality concepts into road network disruption assessments for
635 volcanic eruptions. J Appl. Volcanol. 11, 8, https://doi.org/10.1186/s13617-022-00118-x, 2022.
636 Heiken, G.; Murphy, M.; Hackett, W.; Scott, W.: Volcanic Hazards to Energy Infrastructure-Ash Fallout Hazards and
637 Their Mitigation; World Geothermal Congress: Florence, Italy, pp. 2795–2798, 1995.
638 Hersbach, H., Bell, B., Berrisford, B., Biavati, P., Horányi, A., Muñoz Sabater, J., Nicolas, J., Peubey, C., Radu, R.,
639 Rozum, I., Schepers, D., Simmons, A., Soci, C., Dee, D., and Thépaut, J.: ERA5 hourly data on
640 pressure levels from 1959 to present, 1999–2049, https://doi.org/10.24381/cds.b, 2018.
641 Horwell, C.J. and Baxter, P.J.: The Respiratory Health Hazards of Volcanic Ash: A Review for Volcanic Risk
642 Mitigation. Bulletin of Volcanology, 69, 1-24, http://dx.doi.org/10.1007/s00445-006-0052-y, 2006.
643 Jenkins S.F., Spence R.J.S., Fonseca J.F.B.D., Solidum R.U., Wilson T.M.: Volcanic risk assessment: quantifying
644 physical vulnerability in the built environ- ment. J Volcanol Geotherm Res 276:105–120, 2014.
645 Jenkins, S., Barsotti, S., Hincks, T. K., Neri, A., Phillips, J. C., Sparks, R. S. J., et al.: Rapid emergency assessment of
646 ash and gas hazard for future eruptions at Santorini Volcano, Greece. J. Appl. Volcanol. Soc. Volcanoes 20154:16. doi:
647 10.1186/s13617-015-0033-y, 2015.
648 Johnston, D.M.; Daly, M.: Auckland erupts!!, N. Z. Sci. Mon. 1995, 8, 6–7, 1995.
649 Johnston, D.M.: Physical and Social Impacts of Past and Future Volcanic Eruptions in New Zealand. Ph.D. Thesis,
650 Massey University, Palmerston North, New Zealand, 1997.
651 Labadie, J.R.: Volcanic Ash Effects and Mitigation. Adapted from a Report Prepared in 1983 for the Air Force Office of
652 Scientific Research and the Defence Advanced Research Projects Agency, 1994.
653 Magill, C., Blong, R. and McAneney, J.: VolcaNZ - A volcanic loss model for Auckland, New Zealand, Journal of
654 Volcanology and Geothermal Research 149 (2006) 329–345, 2006.
655 Marzano, F. S., Picciotti, E., Vulpiani, G., Montopoli, M.: Synthetic signatures of volcanic ash cloud particles from X-
656 band dual-polarization radar. IEEE Transactions on Geoscience and Remote Sensing, 50(1), 193–211.
657 https://doi.org/10.1109/TGRS.2011.2159225, 2012.

Marzano, F. S., Mereu, L., Scollo, S., Donnadieu, F., Bonadonna, C.: Tephra mass eruption rate from ground-based X-band and L-band microwave radars during the November 23, 2013 Etna Paroxysm. IEEE Transactions on Geoscience and Remote Sensing, 58(5), 3314–3327, https://doi.org/10.1109/tgrs.2019.2953167, 2020.

Mastin, L. G., Guffanti, M., Servranckx, R., Webley, P., Barsotti, S., Dean, K., et al.: A multidisciplinary effort to assign realistic source parameters to models of volcanic ash-cloud transport and dispersion during eruptions. Journal of Volcanology and Geothermal Research, 186(1–2), 10–21, https://doi.org/10.1016/j.jvolgeores.2009.01.008, 2009.

Mereu, L., Marzano, F. S., Montopoli, M., Bonadonna, C.: Retrieval of tephra size spectra and mass flow rate from C-band radar during the 2010 Eyjafjallajökull eruption, Iceland. IEEE Transactions on Geoscience and Remote Sensing, 53(10), 5644–5660. https://doi. org/10.1109/tgrs.2015.2427032, 2015.

Mereu, L., Scollo, S., Bonadonna, C., Freret-Lorgeril, V., Marzano, F. S.: Multisensor characterization of the incandescent jet region of lava fountain-fed tephra plumes. Remote Sensing, 12(21), 3629. https://doi.org/10.3390/rs12213629, 2020.

Mereu, L., Scollo, S., Bonadonna, C., Donnadieu, F., Freret Lorgeril, V., Marzano, F. S.: Ground-based remote sensing of volcanic mass flow: Retrieval techniques and uncertainty analysis of Mt. Etna eruptions in 2015. IEEE Journal of Selected Topics in Applied Earth Observations and Remote Sensing, 15, 504–518, https://doi.org/10.1109/jstars.2021.3133946, 2022.

Mereu, L., Scollo, S., Garcia, A., Sandri, L., Bonadonna, C., Marzano, F. S.: A new radar-based statistical model to quantify mass eruption rate of volcanic plumes. Geophysical Research Letters, 50, e2022GL100596, https://doi. org/10.1029/2022GL100596, 2023.

Miller, T.P.; Casadevall, T.J.: Volcanic ash hazards to aviation. In Encyclopedia of Volcanoes, 1st ed.; Sigurdsson, H., Houghton, B., Rymer, H., Stix, J., McNutt, S., Eds.; Academic Press: San Diego, CA, USA, pp. 915–930, 1999.

Montopoli, M.: Velocity profiles inside volcanic clouds from three-dimensional scanning microwave dual-polarization Doppler radars. Journal of Geophysical Research: Atmospheres, 121(13), 7881–7900, https: //doi.org/10.1002/2015JD023464, 2016.

Pardini F., De' Michieli Vitturi M., Andronico D., Esposti Ongaro T., Cristaldi A. and Neri A.: Real-time probabilistic assessment of volcanic hazard for tephra dispersal and fallout at Mt. Etna: the 2021 lava fountain episodes, Bulletin of Volcanology, 85:6, https://doi.org/10.1007/s00445-022-01614-z, 2023.

Romeo, F.; Mereu, L.; Scollo, S.; Papa, M.; Corradini, S.; Merucci, L.; Marzano, F.S.: Volcanic Cloud Detection and Retrieval Using Satellite Multisensor Observations. RemoteSens.,15,888, https:// doi.org/10.3390/rs15040888, 2023.

Sarna-Wojcicki, A.M.; Shipley, S.; Waitt, R.B.; Dzurisin, D.; Wood, S.H.: Areal distribution, thickness, mass, volume, and grain size of air-fall ash from the six major eruptions of 1980. In The 1980 Eruptions of Mount Saint Helens; USGS Numbered Series 1250; Lipman, P.W., Mullineaux, D.R., Eds.; U.S. Government Publishing Office: Washington, DC, USA, pp. 577–600, 1981.

Scollo, S., Del Carlo, P., Coltelli, M., Tephra fallout of 2001 Etna flank eruption: Analysis of the deposit and plume dispersion, Journal of Volcanology and Geothermal Research Volume 160, Issues 1–2, 1 February 2007, Pages 147-164, https://doi.org/10.1016/j.jvolgeores.2006.09.007, 2007.

Scollo, S., S. Tarantola, C. Bonadonna, M. Coltelli, and A. Saltelli: Sensitivity analysis and uncertainty estimation for tephra dispersal models, J. Geophys. Res., 113, B06202, doi:10.1029/2006JB004864, 2008a.

Scollo, S., Folch, A., Costa, A.,: A parametric and comparative study of different tephra fallout models, Journal of volcanology and geothermal research 176,199-211, 2008b.

Scollo, S., Prestifilippo, M., Spata, G., D'Agostino, M., Coltelli, M.: Monitoring and forecasting Etna volcanic plumes. Natural Hazards and Earth System Sciences, 9(5), 1573–1585. https://doi.org/10.5194/nhess-9-1573, 2009.

Scollo, S., M. Coltelli, C. Bonadonna, and P. Del Carlo: Tephra hazard assessment at Mt. Etna (Italy), Nat. Hazards Earth Syst. Sci., 13, 3221–3233, doi:10.5194/nhess-13-3221-2013, 2013.

Scollo S., Prestifilippo M., Bonadonna C., Cioni R., Corradini S., Degruyter W., Rossi E., Silvestri M., Biale E., Carparelli G., Cassisi C., Merucci L., Musacchio M. and Pecora E.: Near-Real-Time Tephra Fallout Assessment at Mt. Etna, Italy, Remote Sens., 11, 2987; doi:10.3390/rs11242987, 2019.

Spence, R. J. S., Kelman, I., Baxter, P. J., Zuccaro, G., and Petrazzuoli, S.: Residential building and occupant vulnerability to tephra fall, Natur. Hazards Earth Syst. Sci. 5, 477–494. doi: 10.5194/nhess-5-477-2005.

Taddeucci, J., Edmonds, M., Houghton, B., James, M.R., Vergniolle, S.: Hawaiian and Strombolian Eruptions. The Encyclopedia of Volcanoes; Elsevier Inc.: Amsterdam, The Netherland; University of Rhode Island: Narragansett, RI, USA, pp. 485–503, 2015.

Tadini, A., Gouhier, M., Donnadieu, F., de'Michieli Vitturi, M., & Pardini, F.: Particle sedimentation in numerical modelling: a case study from the Puyehue-Cordón Caulle 2011 eruption with the PLUME-MoM/HYSPLIT models. Atmosphere, 13(5), 784, 2022.

Takishita, K., Poulidis, A. P., & Iguchi, M.: Tephra4D: a python-based model for high-resolution tephra transport and deposition simulations—applications at Sakurajima volcano, Japan. Atmosphere, 12(3), 331, 2021.

Volentik A.C.M., Connor C.B., Connor L.J., Bonadonna C.: Aspects of volcanic hazards assessment for the Bataan nuclear power plant, Luzon Peninsula, Philippines. In: Connor C., Chapman N.A., Connor L. (eds) Volcanic and tectonic hazard assessment for nuclear facilities. Cambridge University Press, Cambridge, 2009.

Vulpiani, G., Ripepe, M., Valade, S.: Mass discharge rate retrieval combining weather radar and thermal camera observations. Journal of Geophysical Research: Solid Earth, 121(8), 5679–5695, https://doi.org/10.1002/2016jb013191, 2016.

Wardman, J. B., Wilson, T., Bodger, P. S., Cole, J. W., and Johnston, D. M.: Investigating the electrical conductivity of volcanic ash and its effects on HV power systems. Phys. Chem. Earth 45–46, 128–145. doi: 10.1016/j.pce.2011.09.003, 2012.

Wilson, L., Parfitt, E.A., Head, J.W.: Explosive volcanic eruptions-VIII. The role of magma recycling in controlling the behaviour of Hawaiian-style lava fountains. Geophys. J. Int., 121, 215–225, 1995.

Wilson, T. M, Stewart, C., Sword-Daniels, V., Leonard, G. S., Johnston, D. M, Cole, J. W., Wardman, J., et al.: Volcanic ash impacts on critical infrastructure. Phys. Chem. Earth 45–46, 5–23. doi: 10.1016/j.pce.2011.06.006, 2012.

Wilson, G.; Wilson, T.M.; Deligne, N.I.; Cole, J.W.: Volcanic hazard impacts to critical infrastructure: A review. J. Volcanol. Geotherm. Res., 286, 148–182, 2014.